



Cite this: *Nanoscale Adv.*, 2021, **3**, 5166

Synthesis and applications of WO_3 nanosheets: the importance of phase, stoichiometry, and aspect ratio

Travis G. Novak,^{†a} Jin Kim,^{†b} Paul A. DeSario  ^c and Seokwoo Jeon  ^{*d}

Tungsten trioxide (WO_3) is an abundant, versatile oxide that is widely explored for catalysis, sensing, electrochromic devices, and numerous other applications. The exploitation of WO_3 in nanosheet form provides potential advantages in many of these fields because the 2D structures have high surface area and preferentially exposed facets. Relative to bulk WO_3 , nanosheets expose more active sites for surface-sensitive sensing/catalytic reactions, and improve reaction kinetics in cases where ionic diffusion is a limiting factor (e.g. electrochromic or charge storage). Synthesis of high aspect ratio WO_3 nanosheets, however, is more challenging than other 2D materials because bulk WO_3 is not an intrinsically layered material, making the widely-studied sonication-based exfoliation methods used for other 2D materials not well-suited to WO_3 . WO_3 is also highly complex in terms of how the synthesis method affects the properties of the final material. Depending on the route used and subsequent post-synthesis treatments, a wide variety of different morphologies, phases, exposed facets, and defect structures are created, all of which must be carefully considered for the chosen application. In this review, the recent developments in WO_3 nanosheet synthesis and their impact on performance in various applications are summarized and critically analyzed.

Received 23rd May 2021
Accepted 5th August 2021

DOI: 10.1039/d1na00384d
rsc.li/nanoscale-advances

1. Introduction

Tungsten trioxide (WO_3) is of interest in a great number of potential applications due to both its intrinsic properties and its wide range of options for chemical/structural modifications. WO_3 is generally eco-friendly, inexpensive, and abundant.¹ Pure WO_3 can be stable or metastable in many phases, including monoclinic, orthorhombic, hexagonal, or cubic, with several hydrated crystalline phases of various stoichiometries

^aNRC Postdoctoral Associate, US Naval Research Laboratory, Washington, D.C., 20375, USA

^bThin Film Materials Research Center, Korea Research Institute of Chemical Technology, Daejeon, 34114, Republic of Korea

^cChemistry Division (Code 6100), U.S. Naval Research Laboratory, Washington, D.C., 20375, USA

^dDepartment of Materials Science and Engineering, KAIST Institute for the Nanocentury, Advanced Battery Center, KAIST, Daejeon, 34141, Republic of Korea.
E-mail: jeon39@kaist.ac.kr

† These authors contributed equally.



Dr Travis Novak is a post-doctoral research associate at the U.S. Naval Research Laboratory (NRL) working in the Surface Chemistry Branch. He received his PhD from the Korean Advanced Institute of Science and Technology (KAIST) under Prof. Seokwoo Jeon, where his research centered on synthesis of 2D materials for energy applications. His current research focuses on developing oxide and metal/oxide nanoarchitectures for environmental remediation catalysts.



Dr Jin Kim received his PhD degree in Materials Science and Engineering from KAIST under supervision of Prof. Seokwoo Jeon. His research field was fabrication of 2D materials including graphene, TMDCs and also TMOs. Currently, he joined the Korea Research Institute of Chemical Technology (KRICT) as a post-doctoral researcher to pioneer various applications of those 2D materials in catalysts, energy storage and sensors.



($\text{WO}_3 \cdot n\text{H}_2\text{O}$) possible as well (Table 1).^{2–4} In addition, WO_3 is generally non-toxic,⁵ and its chemical stability over a wide pH range makes it useful for both liquid and gas phase applications.⁶

Bulk WO_3 typically has a band gap of 2.5–3.0 eV,⁷ and due to considerable absorption of visible light, is one of the most widely explored photocatalysts for solar-driven applications. The WO_3 band gap can be tuned for specific applications by widening through quantum confinement,⁸ or narrowing using oxygen vacancy formation⁹ or heteroatom doping.¹⁰ This versatility has led to research into WO_3 photocatalysts and photoelectrocatalysts focused a wide range of reactions, including water oxidation,^{11–14} water reduction,¹⁵ degradation of organic pollutants,^{16–22} methane conversion,²³ CO_2 reduction,^{24–26} nitrate synthesis,²⁷ and cross-coupling reactions.²⁸ WO_3 has also been extensively studied as an electrocatalyst for the hydrogen evolution reaction (HER).²⁹

For use in sensors, WO_3 is an n-type material that readily chemisorbs various gases,³⁰ creating a charge depletion region and subsequent resistivity change. Similar to the case with photocatalysis, modification of WO_3 morphology³¹ or chemical composition³² can alter its properties for enhancement of gas sensing performance.

Table 1 Phases of WO_3 and $\text{WO}_3 \cdot n\text{H}_2\text{O}$

Phase	Symmetry	Notes ^a
$\delta\text{-WO}_3$	Triclinic	–43 to 17 °C
$\gamma\text{-WO}_3$	Monoclinic	17 to 330 °C
$\beta\text{-WO}_3$	Orthorhombic	330 to 740 °C
$\alpha\text{-WO}_3$	Tetragonal	>720 °C
Cubic WO_3	Cubic	Sub-stoichiometric
h-WO_3	Hexagonal	Metastable at <400 °C
$\text{WO}_3 \cdot 2\text{H}_2\text{O}$	Monoclinic	Layered $\text{WO}_5(\text{OH})_2$ sheets
$\text{WO}_3 \cdot \text{H}_2\text{O}$	Orthorhombic	Corner-sharing $\text{WO}_5(\text{OH})$

^a Temperature ranges are for bulk, stoichiometric WO_3 .⁴



Dr Paul DeSario is a staff scientist at NRL in the Surface Chemistry Branch. He received his BS from Miami University, MS from Lehigh University, and PhD from Northwestern University. He joined NRL as a postdoctoral research associate in 2011 and became a staff scientist in 2014. His research interests include the development of various nanostructures for photocatalytic, electrocatalytic, and thermoelectric applications.

WO_3 is also notable for its ability to intercalate lithium ions (Li^+),³³ a trait that makes it applicable as both an energy storage and electrochromic material. In latter case, the mostly transparent WO_3 becomes opaque upon lithiation due to the transition from W^{6+} to W^{5+} states,³⁴ blocking the majority of visible light in films only \sim 100 nm thick.³⁵ This rapid and reversible optical switching makes WO_3 a leading candidate for next-generation “smart window” technology, where the transparent-to-opaque transition could dramatically reduce heating/cooling costs in buildings.³⁶

The exploitation of WO_3 in nanosheet form has potential benefits for many desired applications, as illustrated in Fig. 1. Nanosheets have an abundance of exposed surface sites compared to bulk materials, beneficial for catalytic or sensing applications alike. The inherent porosity and continuous intercalation paths of nanosheets also allow for easier infiltration of ions, notably Li^+ , making them of an ideal morphology for electrochromic and charge storage devices. In addition, nanosheets can often be easily dispersed in aqueous or organic solvents, allowing for compatibility with techniques such as spin-casting, spray coating, or ink-jet printing.

Despite these advantages, there are still many challenges involved with applications of WO_3 nanosheets, mostly related to synthesis. Unlike intrinsically layered materials such as graphite or transition metal dichalcogenides (TMDCs), WO_3 is not amenable to traditional exfoliation techniques. A wide variety of alternative synthesis techniques have been reported, but these generally struggle to achieve a combination of high aspect ratio, chemical purity, and desired phase.

In this review, we summarize and critically analyse the common techniques recently reported for WO_3 nanosheet synthesis, both top-down (starting from bulk) and bottom-up (starting from smaller precursor molecules). Because the synthesis technique strongly affects the morphology, stoichiometry, and phase of the resulting nanosheet, we also discuss the influence of these factors on the desired application.



Prof. Seokwoo Jeon is currently a Chair professor of Materials Science & Engineering at KAIST, starting his position in 2008. He received BS and MS degrees from Seoul National University and then received his PhD from UIUC in 2006 under the supervision of Prof. John A. Rogers. Later he joined Columbia University as Postdoc Research Fellow at NSEC jointly hired from Prof. Collin Nuckolls, Prof. James Hone, and Prof. Philip Kim. His research goals are exploring novel electronic, mechanical, and optical properties from those nanomaterials and employing those materials in real world application.



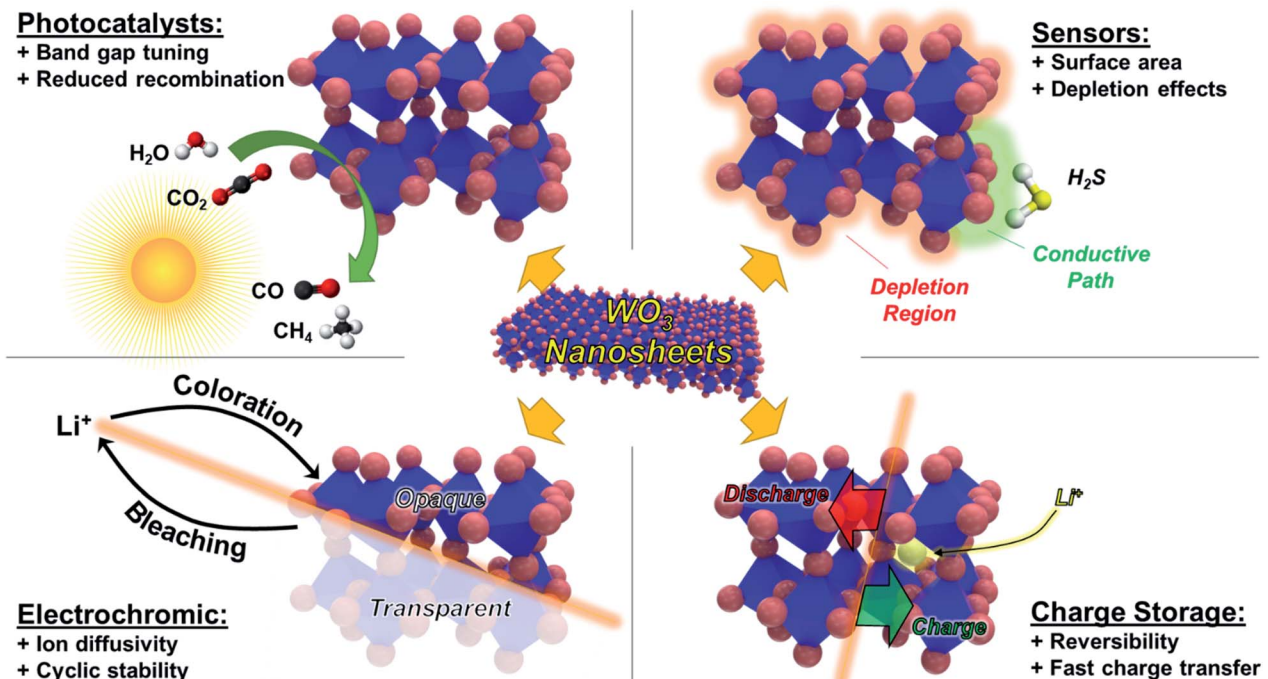


Fig. 1 Schematic showing basic principles of operation for WO_3 in photocatalysts, sensors, electrochromic devices, and charge storage applications, along with the potential advantages provided by the nanosheet morphology.

2. Bottom-up synthesis of WO_3 nanosheets

2.1 Hydrothermal routes

Hydrothermal synthesis typically refers to any method that involves raising the temperature and pressure of a sealed, aqueous solution to yield a desired product.³⁷ This is often considered industrially attractive because it can be a simple, one-step route that is easily scalable, but hydrothermal routes often lack as precise control of morphology and surface chemistry as other methods.

For WO_3 , a wide variety of different shapes can be grown through simple modification of hydrothermal synthesis conditions. Yu *et al.* reported synthesis of hydrated WO_3 nanostructures – 0D nanoparticles, 1D nanorods, 2D nanoplates, and 3D nanoflowers – through a sodium tungstate dihydrate ($\text{Na}_2\text{WO}_4 \cdot 2\text{H}_2\text{O}$) route at 160 °C.³⁸ As shown in Fig. 2, the choice of surfactant determines the morphology of the resulting WO_3 structure. Addition of K_2SO_4 produced nanorods, while oxalic acid produced either nanoplates or nanoflowers, depending on the concentration. The orthorhombic nanoplates were reported to have an average edge length of 300 nm and thickness of 40 nm.³⁸

Variations on this synthetic scheme using $\text{Na}_2\text{WO}_4 \cdot 2\text{H}_2\text{O}$ appear frequently in WO_3 literature.^{39–42} Sodium dodecyl sulfate (SDS) is an anionic surfactant known to functionalize and stabilize nanosheets in solution.⁴³ Addition of SDS to WO_3 hydrothermal routes is common, and it has been asserted that the SDS micelles create additional porosity in WO_3 structures,³⁹ but these often must be thermally removed post-synthesis.

At moderate temperatures, WO_3 prepared through hydrothermal routes tends to be monoclinic or orthorhombic, but can be stabilized in other phases through annealing. Zhang *et al.* synthesized WO_3 nanosheets by a typical hydrothermal route, followed by annealing in N_2 at 350 °C to create hexagonal WO_3 nanosheets.⁴⁰ As with other annealing processes in oxides, this can affect morphology, and likely reduces aspect ratio in the case of nanosheets.

As an alternative to higher temperature routes, Xiao *et al.* showed that addition of Na_2SO_4 stabilizes hexagonal phase WO_3 at a synthesis temperature of only 200 °C.⁴⁴ The nanosheets produced from this route were of relatively high aspect ratio compared to other hydrothermal routes, with an average thickness of 15 nm and lateral sizes appearing to be on the order of 1 μm . Depending on the amount of Na_2SO_4 added, the product appeared either as discrete nanosheets or mesoporous flowers of assembled nanosheets.

Further variations on hydrothermal routes include the use of seeds or templates to create morphological variations. Shi *et al.* synthesized hexagonal WO_3 nanosheets with dominant (100) facets using H_2WO_4 as a precursor and FTO as a seed layer.⁴⁵ This yielded a highly porous assembly, and individual nanosheets appeared to be 100's of nm across.

For template routes, the triblock copolymer Pluronic P123 has been used to synthesize a wide variety of ultrathin oxide nanosheets, where its use promotes lateral growth and reduces agglomeration.⁴⁶ It was later shown for WO_3 that removal of the P123 template at 300 °C results in nanosheets that are thinner (~10 nm) compared to the 20–30 nm of the pristine sheets, while lateral size was maintained at 100's of nm.⁴⁷



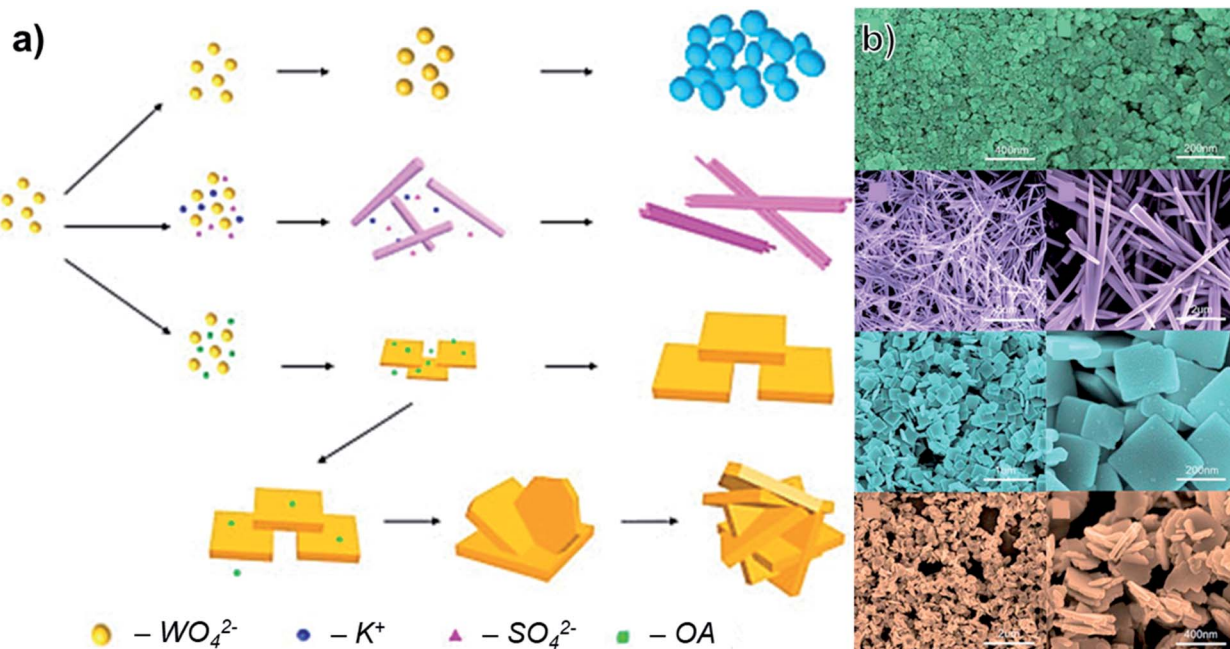


Fig. 2 (a) Schematic of different morphologies of WO_3 produced through a hydrothermal route with variation of precursors (OA: oxalic acid). (b) SEM images of the resulting structures at low and high magnification, adapted with permission from ref. 38, copyright 2016, Elsevier.

Other methods using P123 have demonstrated similarly thin nanosheets. Liang *et al.* used P123 and WCl_6 to synthesize WO_3 nanosheets, finding nanosheets with an average thickness of 4.9 nm and dominant (002) facets.²⁰ A similar method was later used to combine ultra-thin WO_3 nanosheets with C_3N_4 to form a highly porous composite.⁴⁸

2.2 Solution-phase routes at or near room temperature

As their name suggests, the hydrothermal methods described in the previous section use applied heat (most commonly 120–200 °C) to assemble of WO_3 nanostructures from their starting precursors. A closely related class of synthetic technique uses similar starting molecules but relies on acid or base-catalysed reactions rather than thermal stimulus to achieve the desired products. These are often dubbed ‘self-assembly’ or ‘sol-gel’ routes depending on the precursors and methods of assembly, but there is considerable overlap as these methods could also be considered hydrothermal if done in a sealed vessel at elevated temperatures. We will therefore define methods in this section as routes where the primary reactions occur at <100 °C (post-synthesis drying/calcination steps not included).

These low-temperature processes have been used to synthesize WO_3 nanosheets, but typically struggle to achieve a large lateral size. Ahmed *et al.* synthesized WO_3 nanorods and nanosheets through a sol-gel method using $\text{Na}_2\text{WO}_4 \cdot 2\text{H}_2\text{O}$ and HCl .⁴⁹ Post-synthesis calcination at 400, 450, and 500 °C was shown to generate triclinic, orthorhombic, and monoclinic WO_3 , respectively. Thickness was not measured, but lateral size appeared to be on the order of 100’s of nm for the monoclinic nanosheets.

Similar acid-catalysed sol-gel routes can produce a wide variety of nanosheet-like structures. Wang *et al.* demonstrated

that sol-gel synthesized tungstate ($\text{WO}_3 \cdot \text{H}_2\text{O}$) nanosheets that were preferentially [111] oriented would convert to monoclinic [200] oriented WO_3 porous nanosheet arrays (PNAs) upon annealing at 400 °C.⁵⁰ Average thickness was ~20 nm post-annealing, but lateral size of individual nanosheets within the PNA was not clear.

Although not explicitly defined as a sol-gel method, $\text{Na}_2\text{WO}_4 \cdot 2\text{H}_2\text{O}$ with nitric acid (HNO_3) was found to produce polycrystalline, monoclinic nanosheets with crystallite sizes of 22–44 nm after annealing at 500 °C.⁵¹ Substitution of 1–2 at% Sn reduced wrinkles in these nanosheets. The same basic synthesis scheme was later applied to produce Cr-doped WO_3 nanosheets.⁵²

Chen *et al.* demonstrated a similar method for synthesis of WO_3 nanosheets, using one-step method with Na_2WO_4 and HNO_3 at 60 °C.⁵³ Fig. 3a illustrates the formation through self-assembly of the precursor molecules. The authors found that by adding different ratios of sodium oleate (NaOA) and sodium-*n*-octanoate (NaOct) the thickness of WO_3 nanosheets could be controlled. At a NaOct/NaOA mass ratio of 0.04, nanosheets were ~5 nm thick and 10’s of nm in lateral size and of monoclinic phase (Fig. 3b–d).

Another work regarding morphology as a function of additive concentration used oxalic acid in conjunction with $\text{Na}_2\text{WO}_4 \cdot 2\text{H}_2\text{O}$ and HCl .⁵⁴ Optimized conditions yielded monoclinic WO_3 nanosheets with average thickness of ~10 nm and lateral size appearing to be 100’s of nm. The authors proposed that addition of oxalic acid promotes dissolution of $\text{H}_2\text{WO}_4 \cdot n\text{H}_2\text{O}$ precipitates during the growth process, effectively preventing thicker sheets from forming.

In a variation on the acid-catalysed processes, Sánchez-Martínez *et al.* reported ultrasonication-assisted synthesis using



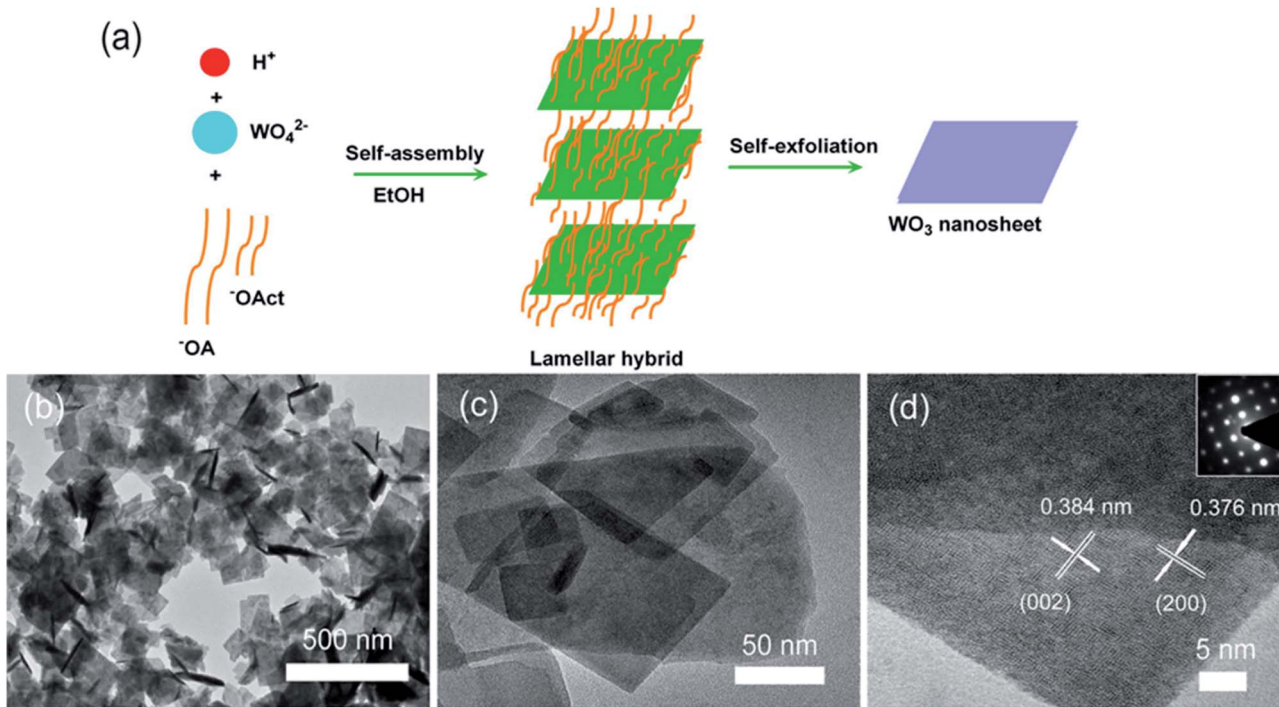


Fig. 3 (a) Schematic of self-assembly. (b–d) SEM, TEM, and HRTEM images of WO_3 nanosheets produced with a NaOct/NaOA mass ratio of 0.04. Reprinted with permission from ref. 53, copyright 2018, Elsevier.

ammonium tungstate hydrate, HNO_3 , and cetyltrimethyl ammonium bromide (CTAB).⁵⁵ The authors asserted that addition of CTAB promotes the formation of nanosheets; samples prepared without CTAB were irregular and of greater thickness. Optimization of CTAB concentration yielded monoclinic WO_3 nanosheets that were 50 nm in average thickness and 100 s of nm in lateral size.

A unique indirect method of obtaining WO_3 nanosheets has been reported through spontaneous conversion of a BaWO_4 -polymer nanohybrid in solution.⁵⁶ Here, a WO_4^{2-} solution was prepared using Na_2WO_4 and added to a solution of barium chloride hexahydrate ($\text{BaCl}_2 \cdot 6\text{H}_2\text{O}$) and polyacrylic acid (PAA). It was asserted that this process formed a BaWO_4 -PAA hybrid that released Ba^{2+} ions into the solution, leaving behind metastable, hexagonal WO_3 nanosheets. Fig. 4 illustrates the interaction of PAA with BaWO_4 and the conversion of WO_4 tetrahedrons to WO_6 octahedrons characteristic of hexagonal WO_3 .

2.3 Other bottom-up routes

While the majority of bottom-up routes utilize precursors dispersed in an aqueous or organic solvent, a few other methods exist based on other techniques. Several of these start from metallic tungsten, which can be oxidized and then assembled into nanosheets through arc-discharge or anodization.

A solid-liquid phase arc discharge route was reported by Chen *et al.* to produce ultra-thin WO_3 nanosheets.²⁴ Here, a tungsten filament at high voltage was brought into contact

with NaNO_3 solution, producing WO_3 nanoparticles in solution. These nanoparticles then preferentially orient and attach along the (100) and (010) axes to form nanosheets, as illustrated in Fig. 5. The rectangular nanosheets produced through this method were ultra-thin, averaging 4.5 nm in height, and 100's of nm in lateral size. A similar technique was later reported to synthesize WO_3 nanoparticles that were oxygen deficient (WO_{3-x}), which the authors attributed to electron bombardment during the arc-discharge.⁵⁷

There also exist several reports of metallic tungsten structures deposited through bottom-up routes that are oxidized to form WO_3 nanosheets. Wisitsora-at *et al.* used RF sputtering to

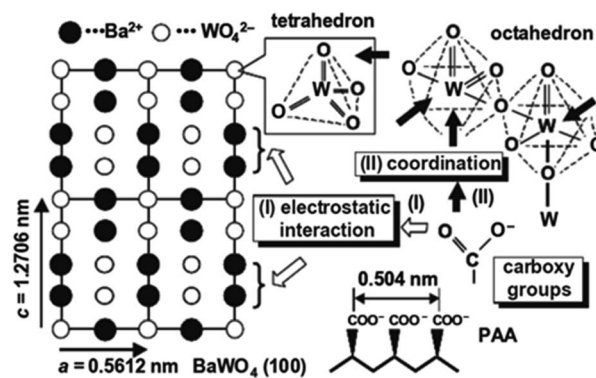


Fig. 4 Illustration of BaWO_4 (100) and the interaction with PAA molecules that leads to formation of octahedral WO_6 . Reprinted with permission from ref. 56, copyright 2006, John Wiley and Sons.



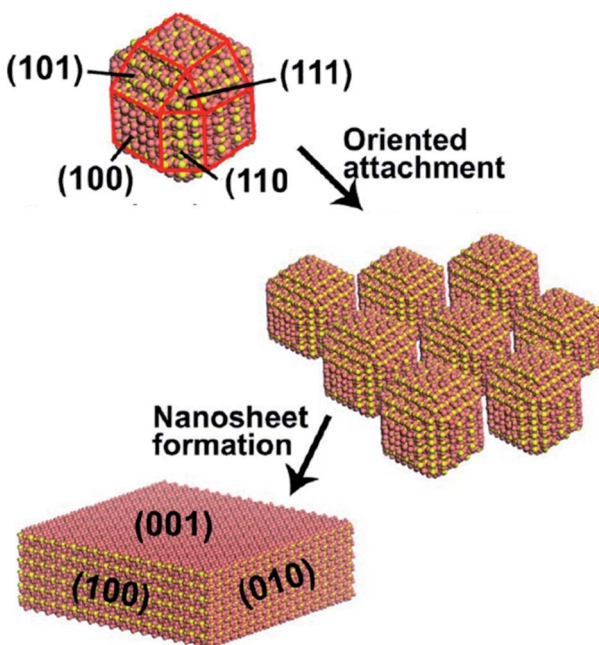


Fig. 5 Schematic of WO_3 formation from smaller nanocrystals produced through solid–liquid phase arc discharge. Reprinted with permission from ref. 24, copyright 2012, American Chemical Society.

deposit a 1 μm thick tungsten film on Al_2O_3 , followed by anodization with HNO_3 at 60 $^\circ\text{C}$ to create films of WO_3 nanosheets.⁵⁸ A similar method had previously been reported to create nanostructured WO_3 films from commercial tungsten foils.⁵⁹ Increasing HNO_3 concentration was found to reduce thickness but also degrade crystallinity, although individual nanosheet dimensions were not specified.

Another report using RF sputtering followed by HNO_3 anodization and annealing at 450 $^\circ\text{C}$ provided more details regarding the morphology of the nanosheet films.⁶⁰ Nanosheets were found to be monoclinic and predominately (002). Average lateral size was 50–500 nm and thickness was 10–50 nm, making the nanosheets similar in both crystallinity and aspect ratio to those grown by solution-phase routes.

While these routes deposited metallic tungsten through bottom-up means and subsequently anodized, it is also possible to create WO_3 nanosheets through direct deposition of the oxide. Luo *et al.* synthesized WO_3 nanosheets through thermal evaporation starting with WO_3 powder to deposit on a glass substrate.⁶¹ The amorphous nanosheets could be separated from the substrate through ultrasonication and were of large lateral size (0.5–10 μm), but thickness was not reported.

An unconventional approach was studied Fang *et al.* using a solid-state mechanochemical reaction induced by ball-milling between $\text{Na}_2\text{WO}_4 \cdot 2\text{H}_2\text{O}$ and oxalate dehydrate ($\text{H}_2\text{C}_2\text{O}_4 \cdot 2\text{H}_2\text{O}$), as illustrated in Fig. 6a.⁶² The resulting $\text{WO}_3 \cdot 2\text{H}_2\text{O}$ monoclinic nanosheets showed a preferential (100) orientation and had an average thickness of 5.67 nm (Fig. 6b). Typical lengths and widths were 50–80 nm and 8–10 nm, respectively.

Overall, there are a wide variety of bottom-up methods for WO_3 synthesis that provide relatively simple and scalable

synthesis and can be tuned to generate different phases of WO_3 . One common drawback of these routes, however, is the relatively low aspect ratio of the nanosheets produced. It is typical to see sizes of 100 s of nm or less with these techniques, potentially limiting the morphological advantages compared to WO_3 produced through methods we will discuss in the following sections.

3. Top-down synthesis of WO_3 nanosheets

While bottom-up methods attempt to synthesize WO_3 from smaller precursor molecules, top-down methods aim to directly cleave nanosheets from the bulk source. In the case of advanced exfoliation techniques, this has been widely developed in order to enhance the aspect ratio while maintaining scalability. For WO_3 this can include either exfoliation of WO_3 , exfoliation of another layered bulk material (WS_2) followed by oxidation, or exfoliation of inherently layered hydrated WO_3 . Among these methods, liquid-phase exfoliation is a promising approach due to not only its scalability but also its simplicity. In this section, we will summarize the progress of top-down synthesis of WO_3 nanosheets, especially in terms of liquid exfoliation, based on different source materials.

3.1 Direct exfoliation of bulk WO_3

Bulk materials could be exfoliated into nanosheets through external stimulation, such as ultra-sonication, and cohesive interaction between the liquid media and the bulk source. This has generated high-quality crystalline nanosheets for a wide variety of van der Waals (VDW) bonded materials, including graphite (graphene),⁶³ TMDCs,⁶⁴ and black phosphorus.⁶⁵ Based on this concept, initial attempts were made by directly exfoliating raw bulk WO_3 in appropriate liquid, but naturally this proved more challenging in a material that was not intrinsically layered.

Perhaps the simplest top-down method reported to date, Szkoda *et al.* refluxed bulk WO_3 powder in water over the course of 10 days at 80 $^\circ\text{C}$, finding that nearly 100% exfoliation occurred and further centrifugation processes were not necessary.⁶⁶ Although some atomically thin structures were observed in TEM, statistical analysis of nanosheets size/thickness was not reported, and lateral size appeared to be limited.

Another route utilizing sonication in aqueous solutions, Guan *et al.* sonicated bulk WO_3 for 48 h in bovine serum albumin (BSA) solution to produce atomically thin WO_3 nanosheets, shown in Fig. 7a.¹⁶ The exfoliation is driven by both aqueous media, which has good cohesive energy with WO_3 , and electrostatic forces caused by BSA molecules. Specifically, the authors observed both theoretically and experimentally that the $-\text{NH}_3^+$ groups of the BSA molecules strongly bind on the negatively charged WO_3 surface in acidic media, making WO_3 nanosheets separate easily from one another through electrostatic force. Because this method is based on electrostatic binding between WO_3 and BSA molecules, the exfoliated monoclinic nanosheets show high crystallinity and long-term

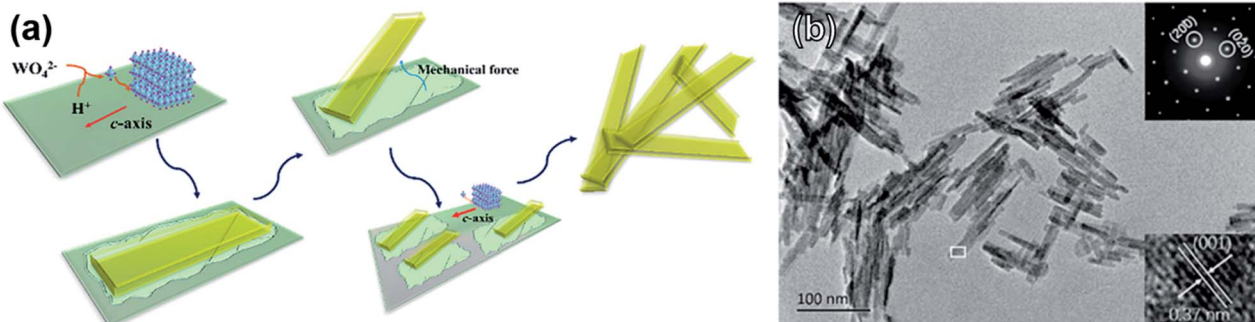


Fig. 6 (a) Schematic of $\text{WO}_3 \cdot 2\text{H}_2\text{O}$ nanosheet formation through a solid-state mechanochemical reaction. (b) TEM image showing nanosheet morphology with inset selected-area diffraction pattern and lattice parameter measurement. Reprinted with permission from ref. 62, copyright 2017 American Chemical Society.

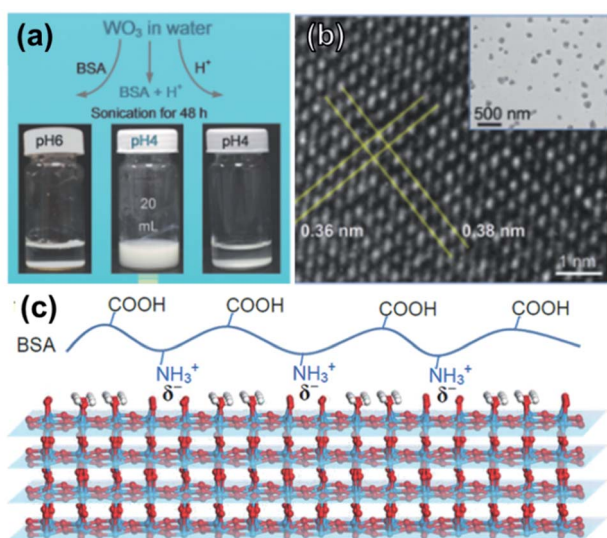


Fig. 7 (a) Optimization of exfoliation/purification for WO_3 exfoliation. (b) HRTEM of a nanosheet with lattice spacing indicated; inset shows typical lateral size of WO_3 nanosheets. (c) Schematic illustration for electrostatic-driven interaction of BSA on WO_3 surface. Reprinted with permission from ref. 16, copyright 2017 John Wiley and Sons.

stability against restacking. After centrifugation at 2000 rpm, 49% of nanosheets were bilayer (2.1 nm thick), but average lateral size was a modest 150 nm.

Although the above works show that it is possible to exfoliate bulk WO_3 into nanostructures, there are clearly severe limitations to these approaches. Because of the strong binding in WO_3 , it is difficult to directionally cleave, resulting in long processing times and nanosheets of low aspect ratio. For improved exfoliation efficiency, there is clearly a need to start with an intrinsically layered material.

3.2 Exfoliation and oxidation from WS_2

Unlike WO_3 , WS_2 is a layered and highly anisotropic material, with strong covalent in-plane bonds and weaker VDW forces out-of-plane. As a result, optimized exfoliation methods can generate WS_2 nanosheets that are >5 nm in thickness and with

lateral sizes that range from 100's of nm to over 1 μm .^{67,68} Naturally, some efforts to synthesize high aspect ratio WO_3 nanosheets have leveraged this approach by exfoliating WS_2 and then attempting to oxidize the WS_2 into WO_3 .

By simply sonicating bulk WS_2 for 4 h in DMF followed by heating at 140 °C, Pan *et al.* showed that oxygen-deficient (WO_{3-x}) dots were formed.⁶⁹ These dots were monoclinic and of extremely small lateral size (2.7 nm on average). Given that the lateral size of the exfoliated WS_2 nanosheets were on the order of microns, it indicates that the uncontrolled oxidation process will break apart otherwise high aspect ratio flakes.

Intercalation can greatly benefit solution-phase exfoliation processes by weakening the interlayer binding forces in VDW materials, allowing for milder sonication conditions. For ionic salts, this can be easily accomplished by heating in an inert environment to allow dissociation of the salt without formation of side products. This approach has been widely reported to generate graphene of higher aspect ratio than other approaches,⁷⁰⁻⁷² and is commonly adapted for other VDW materials such as WS_2 and MoS_2 .⁷³ Fig. 8 illustrates a typical intercalation scheme using *n*-butyllithium (*n*-BuLi), which is a frequently used intercalant for TMDC nanosheet synthesis.⁷⁴

Yim *et al.* utilized this *n*-BuLi intercalation strategy to exfoliate WS_2 , followed by treatment in K_2PdCl_4 at 50 °C.²⁸ This both deposited PdO nanoparticles (~3 nm in diameter) and oxidized the WS_2 nanosheets, forming a $\text{PdO}@\text{WO}_3$ heterostructure. Only trace amounts of sulfur were detected after conversion, and the amorphous WO_3 nanosheets appeared to largely maintain the high aspect ratio of WS_2 .

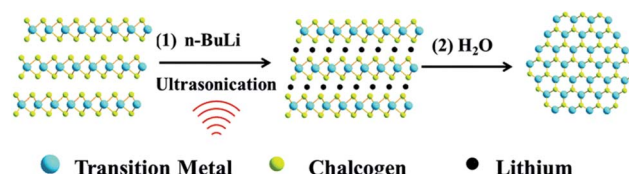


Fig. 8 Intercalation/exfoliation scheme using *n*-BuLi to synthesize TMDC nanosheets. Reprinted with permission from ref. 74, copyright 2016, Royal Society of Chemistry.

Although n -BuLi is the most widely studied, other Li-based salts can be used. Ghorai *et al.* intercalated different lithium salts (I, Br, Cl) in bulk WS_2 to correlate intercalation efficiency to exfoliation yield.⁷⁵ The authors achieved extremely high yield of 19 mg ml⁻¹ by using LiI, which showed the best intercalation efficiency through low lattice energy compared to other salts. When exfoliating WS_2 for WO_3 nanosheet synthesis, there are naturally a similarly wide variety of intercalant options that have been evaluated.

While lithium-based intercalants are widely studied because they share common design principles with electrochromic and charge storage devices based on Li^+ , there are many other ions can readily intercalate into WS_2 , in some cases inducing partial oxidation in addition to interlayer expansion. As shown in Fig. 9a, Zhou *et al.* reported simultaneous exfoliation and oxidation of bulk WS_2 into a partially oxidized WS_2/WO_3 heterostructure, using supercritical CO_2 (sc- CO_2).⁷⁶ Sc- CO_2 could easily permeate into the WS_2 interlayer gallery, which results not only in higher exfoliation efficiency through increased interlayer distance but also oxidation of the WS_2 . Although the sc- CO_2 could be a simple method that could achieve exfoliation and oxidation simultaneously, the WO_3 nanosheet is only partially oxidized, with some WS_2 remaining, and the oxidation becomes especially ineffective for few-layer nanosheets due to limited diffusion of CO_2 beyond the surface layer.

Similarly, Tang *et al.* utilized $FeCl_3$ as both an intercalant and oxidation agent of WS_2 , as shown in Fig. 9b.⁷⁷ During the intercalation process, WS_2 converts to $WOCl_4$ which easily hydrolyses in water to hydrated WO_3 ($WO_3 \cdot H_2O$). After annealing in air at 250 °C, cubic WO_3 nanosheets were formed

that were 3–5 nm thick on average. The authors also found that monoclinic WO_3 nanosheets could be formed by increasing the annealing temperature to 400 °C.

Azam *et al.* used two-step exfoliation and oxidation reaction to produce WO_3 nanosheet using sodium potassium tartrate tetrahydrate.⁷⁸ In this system both the alkali ions and the organic chain intercalate, achieving even larger interlayer distance than intercalation with alkali ions alone and allowing for relatively mild sonication conditions.^{79–81} Due to the four water molecules of the hydrated salt, the WS_2 nanosheet was partially oxidized into WS_xO_y during the intercalation process, a method known to partially oxidize structurally similar MoS_2 .^{82,83} The authors found that the nanosheets were completely oxidized into monoclinic WO_3 after nitric acid treatment, as illustrated in Fig. 9c.⁷⁸ After oxidation, 82% of nanosheets were <10 nm thick and lateral size was 1–20 μm , marking one of the highest average aspect ratios reported to date.

Overall, these methods generally produce the highest aspect ratio WO_3 nanosheets by leveraging the inherent ease of exfoliation of WS_2 . The only notable drawback is process complexity: to achieve fully oxidized WO_3 nanosheets generally requires separate exfoliation and oxidation steps, which tend to make these routes more time consuming than single-step methods.

3.3 Exfoliation of hydrated WO_3

Further research attempted to produce WO_3 intercalation compounds in order to produce highly crystalline WO_3

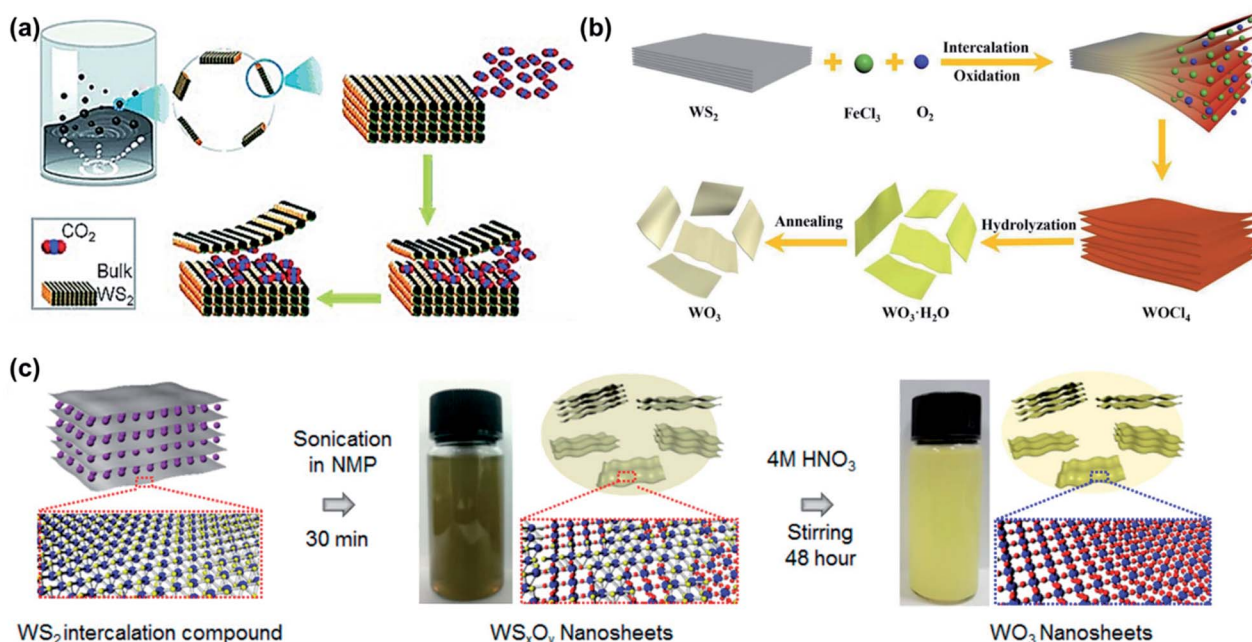


Fig. 9 Examples of exfoliation and oxidation from WS_2 . (a) Supercritical CO_2 used to intercalate and partially oxidize WS_2 , reprinted with permission from ref. 76, copyright 2015 John Wiley and Sons. (b) Use of $FeCl_3$ to intercalate and oxidize WS_2 to $WOCl_4$, followed by hydrolysis in water to yield $WO_3 \cdot H_2O$ and annealing to form WO_3 nanosheets. Reprinted with permission from ref. 77, copyright 2019 John Wiley and Sons. (c) Synthesis of WO_3 nanosheets through intercalation-assisted exfoliation of WS_2 , followed by nitric acid treatment. Reprinted with permission from ref. 78, copyright 2018 American Chemistry Society.



nanosheets without additional oxidation processes. Although the interlayers are strongly bonded through electrostatic interaction, the highly hydrophilic nature of the WO_3 readily harbors water molecules between its interlayers. Compared to bulk WO_3 , layered hydrated WO_3 ($\text{WO}_3 \cdot 2\text{H}_2\text{O}$) can provide structural flexibility to accommodate intercalation-induced strain⁸⁴ and achieve faster intercalation kinetics.⁸⁵ Since intercalation of water in raw bulk WO_3 is difficult, hydrated WO_3 is normally prepared with tungstate precursors, mostly sodium tungstate.

Similar to WS_2 intercalation compounds, Wang *et al.* showed that WO_3 also experiences expansion in interlayer spacing from 3.75 Å to 6.9 Å after water intercalation, which could weaken the binding energy (Fig. 10a).⁸⁶ Kalantar-zadeh *et al.* demonstrated mechanical exfoliation (the scotch-tape method) of ultra-thin nanosheet from hydrated WO_3 , which is not possible from natural bulk WO_3 .⁸⁷ Although this method is not scalable for industrial applications, it served as an important proof of concept that hydrated WO_3 could be exfoliated in ways similar to graphite or other layered materials.

Inspired by this, many turned their attention to utilizing liquid-phase exfoliation for hydrated WO_3 . Zhang *et al.* exfoliated hydrated WO_3 , etching intercalated water molecules with Ar plasma, as shown in Fig. 10b.⁸⁸ The strong etching nature of the Ar-plasma could efficiently exfoliate ultra-thin WO_3 nanosheets with thickness of 1.4 nm while maintaining lateral sizes of 160–180 nm. The harsh etching process also induced numerous oxygen vacancies in the ultra-thin nanosheets.

Liang *et al.* further expanded the interlayer spacing from through intercalation of dodecylamine in hydrated WO_3 (Fig. 10c).⁸⁹ The additional expansion allows higher yield of ultra-thin nanosheets, nearly all with a thickness of 1.4 nm

(corresponding to approximately twice the interlayer distance of adjacent $\text{WO}_3 \cdot \text{H}_2\text{O}$ layers) and lateral size up to 500 nm.

Exfoliation of hydrated WO_3 has been demonstrated to produce nanosheets with monolayer thickness in high yield. Depending on the exfoliation method or co-intercalants other than water, the chemical properties of the WO_3 nanosheets can be additionally tuned as well. However, bulk hydrated WO_3 is typically fabricated on the nanometer scale, making the exfoliated nanosheets also of small lateral size. Nevertheless, the methods introduced above are shown to be efficient for applications that require highly crystalline WO_3 nanosheets.

4. Structure–property relationships for WO_3

The diversity of WO_3 synthesis techniques discussed in previous sections create vastly different materials in terms of phase, morphology, defect structures, *etc.* To better contextualize these synthesis methods for specific applications, it is necessary to briefly discuss how these properties imparted by the specific synthesis methods affect performance. Although we attempt to highlight primarily WO_3 nanosheet based works, in this section some literature regarding other nanostructures or thin films will also be discussed as their insights are often directly applicable to the WO_3 nanosheets as well.

4.1 Effect of morphology and aspect ratio

The term nanosheet implies a true 2D structure, but in the case of WO_3 that is very challenging to achieve. As seen in the discussion of synthesis methods, WO_3 nanosheets often have aspect ratios on the order of 10 : 1 (*i.e.* 100's of nm in later size

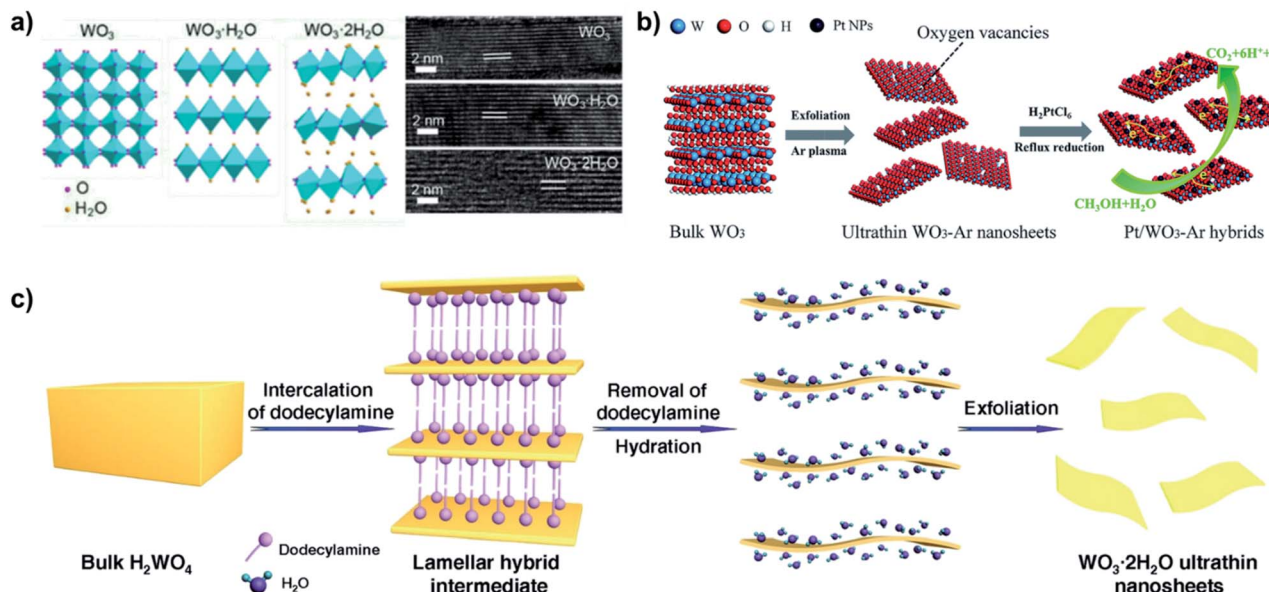


Fig. 10 Examples of interlayer expansion and exfoliation of hydrated WO_3 . (a) Layer expansion of WO_3 upon intercalation with water, reprinted with permission from ref. 86, copyright 2020 American Chemical Society. (b) Exfoliation of hydrated WO_3 using Ar-plasma, followed by deposition of Pt nanoparticles (NPs). Reprinted with permission from ref. 88, copyright 2018 Royal Society of Chemistry. (c) Intercalation and exfoliation of hydrated WO_3 using dodecylamine. Reprinted with permission from ref. 89, Springer-Nature.



and 10's of nm in thickness). This contrasts with other layered materials such as graphene or TMDCs, where aspect ratios of 1000 : 1 or more are possible with advanced exfoliation techniques.^{70–72,90} This is crucial for certain applications as higher aspect ratios can often alter charge transport properties, expose more surface sites, or promote easier ionic diffusion through the structure.

In the case of photocatalysts, nanostructuring WO_3 in nanosheet morphologies can reduce electron–hole recombination, which is detrimental to photoefficiency. The low dimensionality of ultrathin nanosheets ensures that photogenerated charge carriers do not have to traverse large distances to reach the surface,^{11,16,19,20,24} and therefore have an increased probability of reacting with surface adsorbates rather than recombining with electrons.

In addition to reducing charge recombination, morphological modifications of WO_3 can enhance catalysis by leveraging quantum confinement effects to widen its bandgap, shifting the edges of the conduction band (CB) or valence band (VB) for more thermodynamically favourable carrier migration and redox reactions.^{11,17} Although the CB potential of bulk WO_3 is insufficient for O_2 reduction,^{17,18} water reduction,¹⁵ and CO_2 reduction,²⁴ these applications have been realized by shifting the band potentials of WO_3 .

Chen *et al.* demonstrated that the combination of a widened bandgap and a CB shift to more negative potentials in ~4–5 nm thick WO_3 nanosheets provided the necessary thermodynamic power to impart high activity for photocatalytic reduction of CO_2 to CH_4 .²⁴ The stark contrast between photoactivity of WO_3 nanosheets and commercial WO_3 powder is shown in Fig. 11a. Shifting the CB to more negative potentials can also benefit photo-oxidation because as CB electrons more readily react with O_2 they are less likely to recombine with holes.

Although the VB of WO_3 already provides potent oxidative potential, Liu *et al.* demonstrated that the additional overpotential provided by shifting the VB further positive in WO_3 nanosheets improves photoelectrochemical oxygen evolution efficiency relative to bulk WO_3 .¹¹ The quantum size effect is even more pronounced when pores are incorporated into WO_3 nanosheets, further widening its bandgap and improving oxygen evolution activity relative to nonporous WO_3 nanosheets.¹¹

Furthermore, simply the increased surface area afforded by WO_3 nanosheets can benefit photocatalytic applications. Parthibavarman *et al.* analyzed lateral size effect on photocatalytic properties by comparing WO_3 nanosheet and WO_3 nanorod based devices.¹⁹ The larger contact with methylene blue dye provided by larger surface area of WO_3 nanosheet resulted in much better photocatalytic efficiency and stability than WO_3 nanorod did due to more efficient electron transport.

Similarly, thinner WO_3 nanosheets show generally show better performance in sensor applications. As shown in Fig. 11b, Chen *et al.* controlled average thickness of WO_3 nanosheets from 5 nm to 10 nm by adjusting precursor ratio.⁵³ When applied to a triethylamine sensor, the 5 nm WO_3 nanosheet showed 6.4 times better response value than that of 10 nm nanosheet at room temperature.

WO_3 nanosheets have also been found to be superior to other nano-morphologies in sensing applications, implying the importance of the nanosheet morphology. Zhang *et al.* compared volatile organic compound gas sensing properties of WO_3 nanosheets, nanoparticles and nanorods, as shown in Fig. 11c.⁴⁰ The much larger surface area provided from the 2D WO_3 nanosheets showed 9 fold higher selectivity and superior recovery time to those of lower-dimension WO_3 nanorods and nanoparticles.

Finally, there is evidence to suggest electrochromic devices benefit from the high aspect ratio of WO_3 nanosheets as well. The diffusivity of Li^+ is known to be higher at the surface than the interior of WO_3 clusters, making high aspect ratio nanosheets an ideal morphology.⁹¹ As shown in Fig. 11d, Azam *et al.* compared coloration efficiencies of electrochromic devices with WO_3 nanosheets of different thicknesses.⁷⁸ It was found that thinner WO_3 nanosheets have not only better capacity through better packing and higher exposed active surface area, but also better ion diffusivity. Overall, the device based on WO_3 nanosheets with average thickness of less than 10 nm showed 3.43 times higher color modulation and ~46.62% enhancement in response time than those of bulk WO_3 devices. Other works have confirmed these principles for hydrated WO_3 , finding that nanosheet morphologies outperform bulk⁸⁹ or nanorod⁹² expressions of similar chemical composition.

4.2 Effect of phase and preferentially exposed facets

Different phases of WO_3 can both create different adsorption energies for surface reactions and expose different crystal facets. This is particularly important in nanosheets as the facet on the long surfaces of nanosheets have much more surface area than edge surfaces. Often it can be difficult to experimentally determine the exact effect of phase independent of other factors as it is challenging to produce structures that are morphologically identical but of different crystal structures.

Although the overwhelming majority of synthesis methods discussed produce crystalline WO_3 of some form, amorphous WO_3 can be beneficial in certain roles. For refluxed WO_3 nanoflakes, non-crystalline, hydrated WO_3 was found to be superior to crystalline WO_3 in supercapacitors.⁶⁶

In the case of crystalline WO_3 , the exposed facet is particularly important for sensing applications. Song *et al.* compared monoclinic, triclinic, and hexagonal WO_3 nanosheets and found the triclinic phase to be most effective for NO_2 sensing.⁹³ In triclinic WO_3 nanosheets, the (200) surface is terminated by oxygen atoms with a coordination of one (O_{1C}), which are most amenable to redox reactions. The (002) facets of monoclinic WO_3 contain a relatively lower concentration of O_{1C} , while hexagonal (002) facets contain no O_{1C} at all. As seen in Fig. 12, this correlates strongly with their sensing performance for NO_2 .

The oxygen density of preferentially exposed facets also plays an important role in photocatalysts. Here, the high photocatalytic activity of the preferential (001) facet has been attributed to the relative ease with which this surface forms oxygen radicals^{26,94,95} and its low energy barrier for water oxidation.⁹⁴



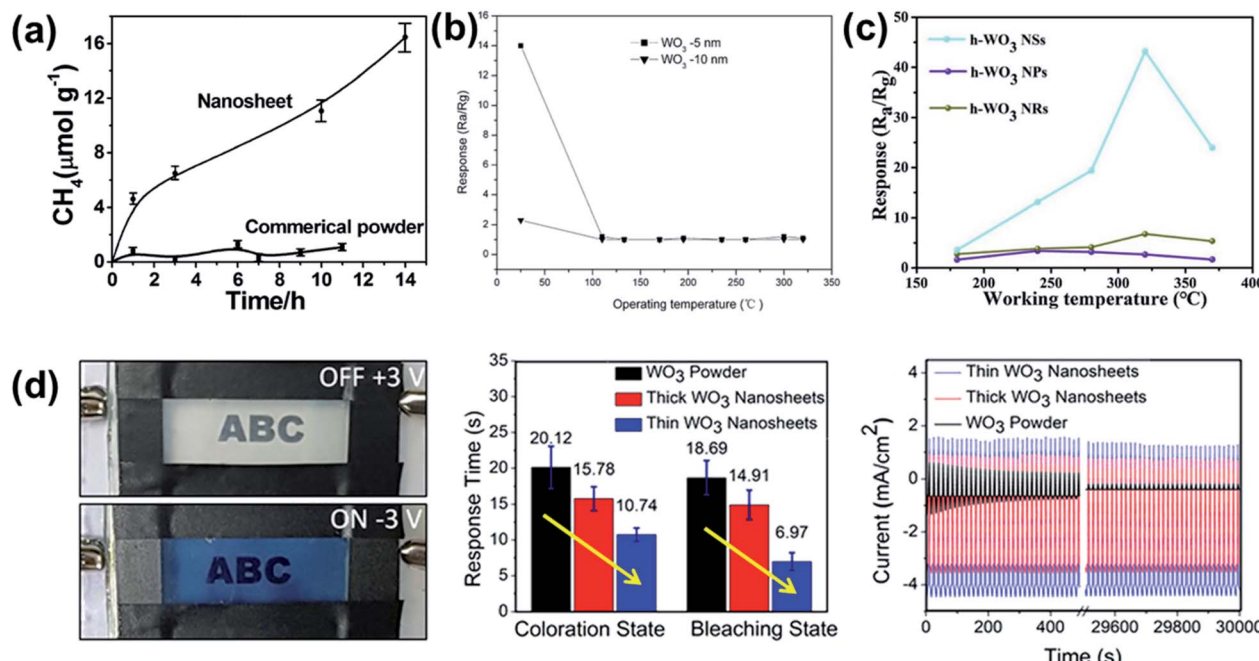


Fig. 11 Effect of morphology for various WO_3 applications. (a) Comparison of nanosheets vs. commercial powder WO_3 for reduction of CO_2 to CH_4 , reprinted with permission from ref. 24, copyright 2012 American Chemical Society. (b) Response time of WO_3 nanosheets with 5 nm and 10 nm average thickness. Reprinted with permission from ref. 53, copyright 2018, Elsevier. (c) Comparison of WO_3 nanosheets (NSs), nanoparticles (NPs) and nanorods (NRs) responses towards 50 ppm of ethylbenzene vapor. Reprinted with permission from ref. 40, copyright 2019, Elsevier. (d) Photographs of on and off states of WO_3 nanosheet based electrochromic device and effect of WO_3 thickness of electrochromic response times and stability. Reprinted with permission from ref. 78, copyright 2018, American Chemical Society.

In electrochromic applications, there are reports of high-performance electrochromic devices from a wide variety of different WO_3 phases. Earlier works regarding electrochromic WO_3 asserted that while amorphous WO_3 could achieve high initial values of coloration efficiency, some crystallinity was

necessary for cyclic stability,^{96,97} as shown in Fig. 13. At least one recent report, however, has found reasonable stability from mesoporous amorphous WO_3 ,⁹⁸ which could be attributed to the ability of the highly porous structure to prevent stress accumulation upon Li^+ insertion.

Djaoued *et al.* used sol-gel synthesis to create porous electrochromic WO_3 thin films of three different phases: hexagonal, monoclinic, and orthorhombic.⁹⁹ There was minimal difference observed in optical modulation between the three films; all achieved optical modulation of at least 70%, indicating that Li^+ produces similar effects in all three structures. The authors did not evaluate switching times or cyclic stability, however, so it is possible that certain phases still have electrochromic advantages in these parameters.

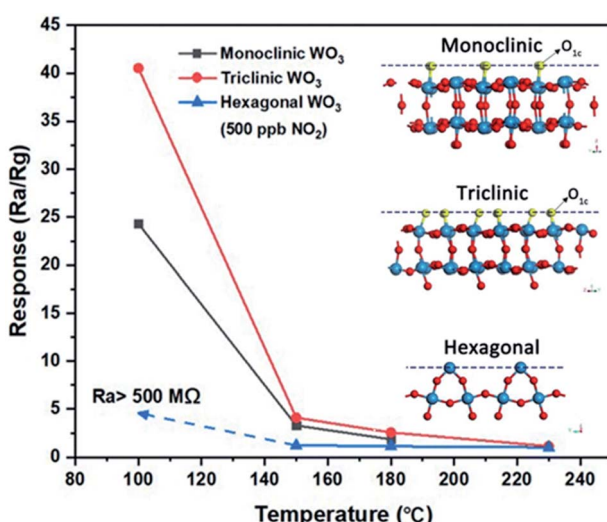


Fig. 12 Effect of WO_3 crystal structure on sensing performance of NO_2 . Inset shows the crystal structures with density of single coordinated oxygen atoms (O_{1c}) on the exposed facet. Reprinted with permission from ref. 93, copyright 2020, Springer-Nature.

4.3 Effect of oxygen vacancies

Although typically labelled simply ' WO_3 ', it is rare for the stoichiometry to be exactly 3 : 1; as-synthesized WO_3 is typically slightly oxygen deficient. Promoting and tuning the oxygen vacancy (O_{vac}) concentration can enhance various properties, notably visible light absorption for photoactivity¹⁰⁰ and adsorption energy of various molecules for catalytic or sensing applications.¹⁰¹

Incorporating oxygen vacancies or other defects into nanosheet surfaces can further improve their photocatalytic activity. Oxygen deficient WO_3 can exhibit localized surface plasmon resonance (LSPR) in the IR region, improving light harvesting as



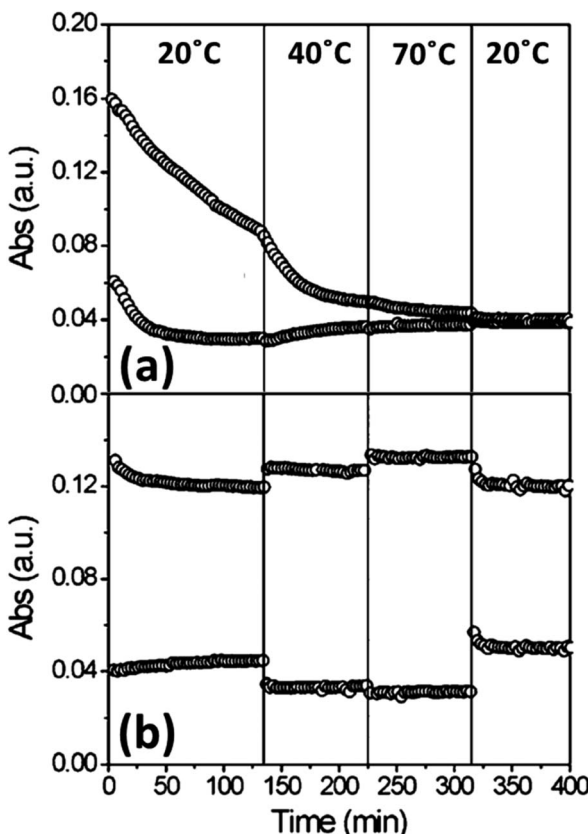


Fig. 13 Absorption change of amorphous (a) and crystalline (b) WO_3 thin films at various temperatures over time. Reprinted with permission from ref. 96, copyright 2007, American Chemical Society.

shown in Fig. 14a.¹⁰² More commonly, the benefit of oxygen-vacancies on the photocatalytic activity of WO_3 nanosheets has been ascribed to bandgap narrowing, thus improving visible-light utilization,¹² and formation of highly active superoxide radicals at vacancy sites.²¹ Fig. 14b shows the effect of oxygen vacancy induced band gap narrowing on visible light photocurrents in Pt/ WO_3 nanosheets.¹⁰³

Creating voids in the nanosheet surface, referred to as nanopores¹¹ or “potholes”,²⁷ improves carrier separation and migration and promotes adsorption and activation of chemical species. Holes traversing along the (001) surface of porous nanosheets can find pore-adsorbed reactants before they have the opportunity to recombine.¹¹ A higher degree of band bending in porous nanosheets relative to nonporous nanosheets accounts for the improved charge transfer resistance in the former.¹¹ Pothole voids expose more dangling surface oxygens than defect-free surfaces and thus provide electron rich sites for adsorption and activation of chemical species.²⁷ The electron-rich pothole defects in WO_3 nanosheets have been implicated in adsorbing and activating N_2 , thus forming a metastable N_2 intermediate that is prone to conversion to NO , while no such intermediate forms in pothole-free WO_3 .²⁷

For electrocatalysts, Kong *et al.* studied the effect on oxygen vacancies in WO_3 nanosheets for N_2 reduction to NH_3 .¹⁰⁴ Nanosheets were prepared through a typical hydrothermal

method, followed by annealing at 400°C in an N_2 atmosphere to produce oxygen-vacancy rich nanosheets (R- WO_3 NSs), or the same temperature in air to produce nanosheets deficient in oxygen vacancies (D- WO_3 NSs). A TEM image highlighting the lattice distortions induced by oxygen vacancies is shown in Fig. 14c. Oxygen vacancies in R- WO_3 NSs were asserted to promote additional adsorption sites for N_2 or reduce electron transfer resistance, resulting in Faradaic efficiency (FE) that was far greater than D- WO_3 NSs (Fig. 14d).

The ability of oxygen vacancies to modify adsorption characteristics of gases also can benefit WO_3 for sensing applications. In the case of oxidizers such as NO_2 , the electrophilic gas can be adsorbed more effectively since surface oxygen vacancies act as n-type dopants.⁴⁷ Improved adsorption of NO_2 in oxygen vacancy rich WO_3 nanostructures had been previously predicted through DFT analysis,¹⁰⁵ and has since been mechanistically studied over a various WO_3 morphologies.¹⁰⁶

For detection of reducing gases it could be expected that the oxygen vacancies would have the opposite effect, but this is not always the case. It was observed by Rahmani *et al.* that detection of H_2 was improved after compensation of crystal defects like oxygen vacancies,⁶⁰ but for other reducing gases such as H_2S ¹⁰¹ and NH_3 (ref. 107) there is some evidence to the contrary. In the case of ammonia sensing this was attributed to band gap narrowing causing easier injections of electrons from ammonia to the CB of WO_3 .¹⁰⁷

While oxygen vacancies are beneficial for certain catalytic and sensing applications, for electrochromic applications there are conflicting reports regarding their effects. For WO_3 nanosheets, Zhou *et al.* reported that hydrogen treatment to induce oxygen vacancies produced electrochromic films that were superior in both contrast ratio and switching time to pristine WO_3 .¹⁰⁸ Fig. 14e and f show the difference between annealed WO_3 and hydrogenated WO_3 , respectively. The authors posited that the oxygen vacancies could be helpful for Li^+ insertion and extraction. Other oxygen-deficient WO_3 nanostructures have similarly shown short coloration/bleaching times.¹⁰⁹

A later study, however, found that oxygen vacancies are not necessarily beneficial for electrochromic films.¹¹⁰ Here, three different films were studied: as-deposited, annealed in O_2 , and annealed in Ar. The as-deposited amorphous films showed the best ΔT (87%) but poor cyclic stability, while the films annealed in Ar (which were crystalline, but with abundant oxygen vacancies) was the worst (51%). WO_3 annealed in O_2 showed the best cyclic stability and still retained moderate contrast (71%). This shows that while amorphous regions or other structural defects may boost electrochromic performance, oxygen vacancies specifically do not.

4.4 WO_3 nanosheet based composites

The intrinsic properties of WO_3 make it amenable to hybridization with various other materials to modify its electronic or optical properties. WO_3 nanosheets can be particularly well-suited to these roles as their high surface area allows for easy surface doping with other chemical moieties and/or intimate contact with other nanostructures.



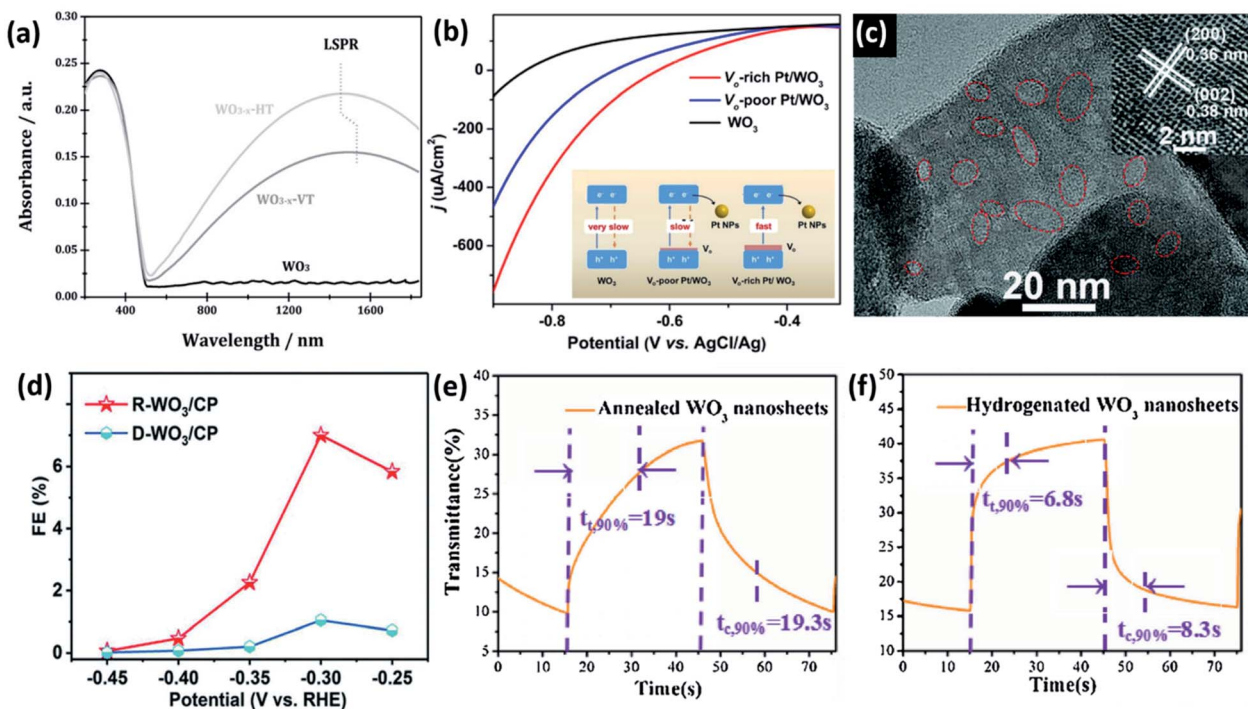


Fig. 14 Impact of oxygen vacancies of WO₃. (a) LSPR formation in oxygen vacancy rich WO₃ nanosheets. Reprinted with permission from ref. 102, copyright 2015, John Wiley and Sons. (b) Band gap narrowing and improved photocurrent induced by oxygen vacancy formation. Adapted from ref. 103, copyright 2020 Elsevier. (c) TEM image of oxygen vacancy rich WO₃ nanosheets (R-WO₃) and (d) comparison of FE for reduction of N₂ to NH₃. Reprinted with permission from ref. 104, copyright 2019, Royal Society of Chemistry. (e) Electrochromic response of annealed WO₃ nanosheets vs. (f) hydrogenated WO₃ nanosheets. Reprinted with permission from ref. 108, copyright 2017 Elsevier.

Rapid recombination of electrons and holes in WO₃ photocatalysts has been thwarted by transferring charges across heterojunctions to metal nanoparticles^{12,17} or other semiconductors.^{15,18,25} Electron transfer between WO₃ nanosheets and Pt¹⁷ or Ag¹² nanoparticles is demonstrated to reduce recombination of photogenerated electron–hole pairs and allow photo-generated holes to more efficiently drive oxidation of tetracycline¹⁷ or water,¹² respectively. Fig. 15a shows the total organic carbon (TOC) removal curves of Pt/WO₃.¹⁷

Paired with other semiconductors, the strong oxidizing power of WO₃ can be coupled with the strong reducing power of a reduction catalyst in a direct Z-scheme heterojunction composite (note: this sub-type of Z-scheme photocatalyst has recently been re-named S-scheme to avoid confusion with other types of Z-scheme photocatalysts^{15,111}). In this configuration, when both semiconductors are excited, the VB holes of the reduction catalyst react with CB electrons in WO₃, thus separating VB holes in WO₃ from CB electrons in the reduction catalyst.

The strong oxidizing power of WO₃ has been combined with the superior reducing power of CdS,¹⁸ g-C₃N₄,¹⁵ or iron phthalocyanine (FePc)²⁵ to promote efficient photocatalytic/photocatalytic ciprofloxacin degradation, water reduction, and CO₂ reduction, respectively. This type of S-scheme heterojunction is particularly effective when coupling 2D materials due to the large interfacial contact area, such as is realized between ultrathin WO₃ nanosheets and g-C₃N₄ nanosheets.¹⁵ Fig. 15b shows the band structure of WO₃/g-C₃N₄ for S-scheme H₂ photocatalysts.

Similar compositing strategies for WO₃ nanosheet based sensors can benefit performance by altering the electronic structure. Pairing n-type WO₃ nanosheets with p-type nanosheets, such as MoS₂ (ref. 112) or WS₂,¹¹³ creates a strong depletion region with a built-in field across the junction which is highly sensitive to charge transfer events on the surface. Fig. 15c shows the superior sensing response of MoS₂/WO₃ compared to pure MoS₂ or WO₃ for ammonia sensing. The same concept has been utilized in tungsten oxysulfide nanosheets to create strong depletion regions within the nanosheet surface.¹¹⁴

Nanosheets can also be decorated with other oxides to promote oxygen vacancies or other defect species that are sensitive to the target species.^{115–117} Fig. 15d shows the response of pure WO₃ and pure SnO₂ compared to SnO₂-decorated WO₃ nanosheets for detection of acetone vapor.¹¹⁶ The authors asserted that lattice distortion at the SnO₂–WO₃ interface creates dangling bonds and non-uniform electron distributions that act as favourable adsorption sites.

In charge storage applications, compositing strategies for WO₃ often focus on pairing the normally insulating oxide with a more conductive material to alleviate charge transport issues. WO₃ paired with graphene/rGO frequently appears in literature for both supercapacitors^{118,119} and Li-ion battery anodes,^{120,121} in both cases providing faster charge transport and improved stability over pure WO₃.

WO₃ has also been combined with a newly explored class of 2D materials – MXene – in a similar composite concept.¹²²

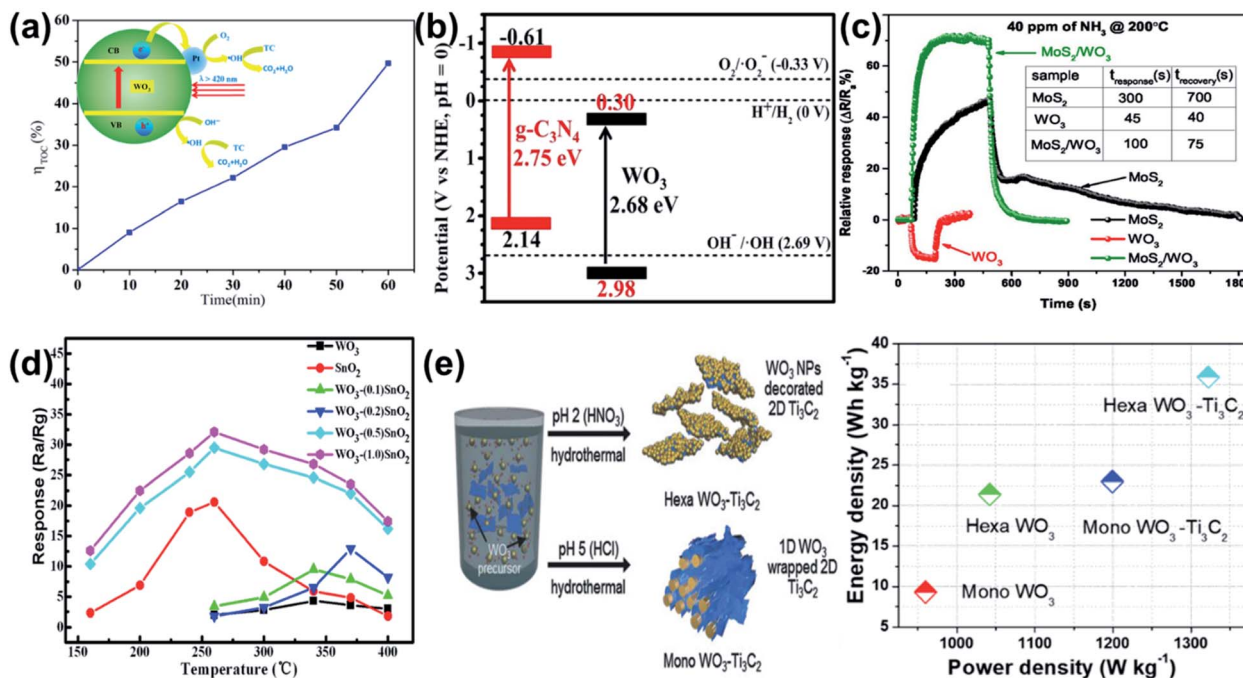


Fig. 15 Compositing/hybridization examples for WO_3 . (a) Removal of tetracycline with Pt NP decorated WO_3 nanosheets, with inset showing the mechanism of charge transfer. Reprinted with permission from ref. 17, copyright 2014, American Chemical Society. (b) Band diagram of $\text{g-C}_3\text{N}_4$ - WO_3 for S-scheme H_2 photocatalysts. Reprinted from ref. 15, copyright 2019 Elsevier. (c) Response over time of MoS_2 , WO_3 , and MoS_2/WO_3 to ammonia. Reprinted with permission from ref. 112, copyright 2021, American Chemical Society. (d) Response of WO_3 , SnO_2 , and various weight loadings of SnO_2 on WO_3 vs. temperature. Reprinted with permission from ref. 116, copyright 2018 Elsevier. (e) Schematic for formation of WO_3 - Ti_3C_2 hybrids and the energy density/power density plot for their use in a supercapacitor. Reprinted with permission from ref. 122, copyright 2018 John Wiley and Sons.

MXene sheets (Ti_3C_2) were mixed into a standard hydrothermal WO_3 synthesis procedure. Depending on the pH of the solution, this method either generated nanorod-like monoclinic WO_3 hybrids (Mono WO_3 - Ti_3C_2), or nanosheet-like hexagonal WO_3 on Ti_3C_2 (Hexa WO_3 - Ti_3C_2). Fig. 15e shows the schematic for synthesis and the effect on supercapacitor performance metrics (power density and energy density), where the Hexa WO_3 - Ti_3C_2 outperforms Mono WO_3 - Ti_3C_2 and either of the pure materials. The effect was attributed to both improved surface area of the nanosheet-like structures as well as intimate contact providing faster ionic movement between WO_3 and Ti_3C_2 .

Although by no means a comprehensive list of all WO_3 nanosheet composites reported in the literature, this provides a sampling of many of the key concepts frequently utilized. Nanosheet expressions of WO_3 can be easily decorated with NPs to either modify their visible light response or tune the adsorption energy for photocatalytic or sensing applications. The combination of WO_3 nanosheets with other 2D materials (graphene, TMDCs, or MXene) is also widely studied to either create depletion regions at the n-type/p-type boundary or facilitate charge transfer.

5. Conclusions

The literature summarized and reviewed here shows the tremendous amount of research interest that WO_3 nanosheets have garnered in recent years. For photocatalytic, sensing,

electrochromic, and charge storage applications, WO_3 nanosheets provide significant advantages over bulk counterparts, and in many cases advantages over other nano-morphologies as well. Because WO_3 is not intrinsically layered, synthesis of high-aspect ratio nanosheets is non-trivial, and as such there is great diversity in their production. Bottom-up methods of various chemistries can successfully synthesize WO_3 nanosheets in simple, one-step methods, but generally struggle to achieve high aspect ratios. Top-down methods, in particular intercalation-assisted exfoliation of WS_2 followed by oxidation, provide a promising alternative for applications which benefit from nanosheets with larger lateral sizes and higher aspect ratios. Both types of synthesis offer many variations in terms of phase and stoichiometry that can be further exploited to fit the target application.

Conflicts of interest

There are no conflicts to declare.

Acknowledgements

T.G.N. gratefully acknowledges the National Research Council for support through a Naval Research Laboratory/National Research Council Postdoctoral Associateship.

Notes and references

1 C. C. Mardare and A. W. Hassel, *Phys. Status Solidi A*, 2019, **216**, 1900047.

2 C. Chacón, M. Rodríguez-Pérez, G. Oskam and G. Rodríguez-Gattorno, *J. Mater. Sci.: Mater. Electron.*, 2015, **26**, 5526–5531.

3 G. N. Kustova, Y. A. Chesalov, L. M. Plyasova, I. Y. Molina and A. I. Nizovskii, *Vib. Spectrosc.*, 2011, **55**, 235–240.

4 H. Zheng, J. Z. Ou, M. S. Strano, R. B. Kaner, A. Mitchell and K. Kalantar-zadeh, *Adv. Funct. Mater.*, 2011, **21**, 2175–2196.

5 I. Angela, T. Tiina, V. Meeri, V. Heiki, K. Aleksandr, S. Mariliis, P. Suman, M. Lutz, H. Margit, K. Vambola, S. Ruth and K. Anne, *Curr. Top. Med. Chem.*, 2015, **15**, 1914–1929.

6 L. Santos, J. P. Neto, A. Crespo, D. Nunes, N. Costa, I. M. Fonseca, P. Barquinha, L. Pereira, J. Silva, R. Martins and E. Fortunato, *ACS Appl. Mater. Interfaces*, 2014, **6**, 12226–12234.

7 P. Dong, G. Hou, X. Xi, R. Shao and F. Dong, *Environ. Sci.: Nano*, 2017, **4**, 539–557.

8 D. Tanaka, Y. Oaki and H. Imai, *Chem. Commun.*, 2010, **46**, 5286–5288.

9 M. Gillet, C. Lemire, E. Gillet and K. Aguir, *Surf. Sci.*, 2003, **532–535**, 519–525.

10 S. S. Kalanur, *Catalysts*, 2019, **9**, 456.

11 Y. Liu, L. Liang, C. Xiao, X. Hua, Z. Li, B. Pan and Y. Xie, *Adv. Energy Mater.*, 2016, **6**, 1600437.

12 Y. Ren, C. Li, Q. Xu, J. Yan, Y. Li, P. Yuan, H. Xia, C. Niu, X. Yang and Y. Jia, *Appl. Catal., B*, 2019, **245**, 648–655.

13 J. J. Zhang, P. Zhang, T. Wang and J. L. Gong, *Nano Energy*, 2015, **11**, 189–195.

14 J. Y. Zheng, G. Song, J. S. Hong, T. K. Van, A. U. Pawar, D. Y. Kim, C. W. Kim, Z. Haider and Y. S. Kang, *Cryst. Growth Des.*, 2014, **14**, 6057–6066.

15 J. W. Fu, Q. L. Xu, J. X. Low, C. J. Jiang and J. G. Yu, *Appl. Catal., B*, 2019, **243**, 556–565.

16 G. Guan, J. Xia, S. Liu, Y. Cheng, S. Bai, S. Y. Tee, Y.-W. Zhang and M.-Y. Han, *Adv. Mater.*, 2017, **29**, 1700326.

17 G. Zhang, W. Guan, H. Shen, X. Zhang, W. Fan, C. Lu, H. Bai, L. Xiao, W. Gu and W. Shi, *Ind. Eng. Chem. Res.*, 2014, **53**, 5443–5450.

18 X. Liu, Y. Yan, Z. Da, W. Shi, C. Ma, P. Lv, Y. Tang, G. Yao, Y. Wu, P. Huo and Y. Yan, *Chem. Eng. J.*, 2014, **241**, 243–250.

19 M. Parthibavarman, M. Karthik and S. Prabhakaran, *Vacuum*, 2018, **155**, 224–232.

20 Y. Liang, Y. Yang, C. Zou, K. Xu, X. Luo, T. Luo, J. Li, Q. Yang, P. Shi and C. Yuan, *J. Alloys Compd.*, 2019, **783**, 848–854.

21 M. M. Zhang, C. Lai, B. S. Li, D. L. Huang, S. Y. Liu, L. Qin, H. Yi, Y. K. Fu, F. H. Xu, M. F. Li and L. Li, *J. Colloid Interface Sci.*, 2019, **556**, 557–567.

22 D. Q. Zhang, S. L. Wang, J. Zhu, H. X. Li and Y. F. Lu, *Appl. Catal., B*, 2012, **123**, 398–404.

23 J. Ma, K. K. Mao, J. X. Low, Z. H. Wang, D. W. Xi, W. Q. Zhang, H. X. Ju, Z. M. Qi, R. Long, X. J. Wu, L. Song and Y. J. Xiong, *Angew. Chem., Int. Ed.*, 2021, **60**, 9357–9361.

24 X. Chen, Y. Zhou, Q. Liu, Z. Li, J. Liu and Z. Zou, *ACS Appl. Mater. Interfaces*, 2012, **4**, 3372–3377.

25 B. Li, L. Q. Sun, J. Bian, N. Sun, J. W. Sun, L. Q. Chen, Z. J. Li and L. Q. Jing, *Appl. Catal., B*, 2020, 270.

26 F. Q. Zhan, W. H. Liu, W. Z. Li, J. Li, Y. H. Yang, Q. Liu, Y. M. Li and X. D. Tang, *J. Mater. Sci.: Mater. Electron.*, 2017, **28**, 13836–13845.

27 Y. Liu, M. Cheng, Z. He, B. Gu, C. Xiao, T. Zhou, Z. Guo, J. Liu, H. He, B. Ye, B. Pan and Y. Xie, *Angew. Chem., Int. Ed.*, 2019, **58**, 731–735.

28 D. Yim, F. Raza, J. H. Park, J.-H. Lee, H.-I. Kim, J.-K. Yang, I.-J. Hwang and J.-H. Kim, *ACS Appl. Mater. Interfaces*, 2019, **11**, 36960–36969.

29 Y. Li, X. Zhai, Y. Liu, H. Wei, J. Ma, M. Chen, X. Liu, W. Zhang, G. Wang, F. Ren and S. Wei, *Frontiers in Materials*, 2020, **7**, 105.

30 H. Long, W. Zeng and H. Zhang, *J. Mater. Sci.: Mater. Electron.*, 2015, **26**, 4698–4707.

31 C. Dong, R. Zhao, L. Yao, Y. Ran, X. Zhang and Y. Wang, *J. Alloys Compd.*, 2020, **820**, 153194.

32 S. Bai, Y. Ma, X. Shu, J. Sun, Y. Feng, R. Luo, D. Li and A. Chen, *Ind. Eng. Chem. Res.*, 2017, **56**, 2616–2623.

33 C. O. Avellaneda and L. O. S. Bulhões, *Solid State Ionics*, 2003, **165**, 59–64.

34 S.-H. Lee, H. M. Cheong, J.-G. Zhang, A. Mascarenhas, D. K. Benson and S. K. Deb, *Appl. Phys. Lett.*, 1999, **74**, 242–244.

35 Y. Zhen, B. P. Jelle and T. Gao, *Analytical Science Advances*, 2020, **1**, 124–131.

36 B. P. Jelle, A. Hynd, A. Gustavsen, D. Arasteh, H. Goudey and R. Hart, *Sol. Energy Mater. Sol. Cells*, 2012, **96**, 1–28.

37 S. Feng and R. Xu, *Acc. Chem. Res.*, 2001, **34**, 239–247.

38 Y. Yu, W. Zeng, M. Xu and X. Peng, *Phys. E*, 2016, **79**, 127–132.

39 J. Shi, Z. Cheng, L. Gao, Y. Zhang, J. Xu and H. Zhao, *Sens. Actuators, B*, 2016, **230**, 736–745.

40 D. Zhang, Y. Fan, G. Li, Z. Ma, X. Wang, Z. Cheng and J. Xu, *Sens. Actuators, B*, 2019, **293**, 23–30.

41 O. O. Abe, Z. Qiu, J. R. Jinschek and P.-I. Gouma, *Sensors*, 2021, **21**, 1690.

42 Y. Wicaksana, S. Liu, J. Scott and R. Amal, *Molecules*, 2014, **19**, 17747–17762.

43 B. Meschi Amoli, J. Trinidad, G. Rivers, S. Sy, P. Russo, A. Yu, N. Y. Zhou and B. Zhao, *Carbon*, 2015, **91**, 188–199.

44 W. Xiao, W. Liu, X. Mao, H. Zhu and D. Wang, *J. Mater. Chem. A*, 2013, **1**, 1261–1269.

45 W. Shi, X. Guo, C. Cui, K. Jiang, Z. Li, L. Qu and J.-C. Wang, *Appl. Catal., B*, 2019, **243**, 236–242.

46 Z. Sun, T. Liao, Y. Dou, S. M. Hwang, M.-S. Park, L. Jiang, J. H. Kim and S. X. Dou, *Nat. Commun.*, 2014, **5**, 3813.

47 Z. Wang, D. Wang and J. Sun, *Sens. Actuators, B*, 2017, **245**, 828–834.

48 D. Wang, S. Huang, H. Li, A. Chen, P. Wang, J. Yang, X. Wang and J. Yang, *Sens. Actuators, B*, 2019, **282**, 961–971.



49 B. Ahmed, S. Kumar, A. K. Ojha, P. Donfack and A. Materny, *Spectrochim. Acta, Part A*, 2017, **175**, 250–261.

50 M. Wang, Y. Wang, X. Li, C. Ge, S. Hussain, G. Liu and G. Qiao, *Sens. Actuators, B*, 2020, **316**, 128050.

51 S. B. Upadhyay, R. K. Mishra and P. P. Sahay, *Sens. Actuators, B*, 2014, **193**, 19–27.

52 S. B. Upadhyay, R. K. Mishra and P. P. Sahay, *Ceram. Int.*, 2016, **42**, 15301–15310.

53 G. Chen, X. Chu, H. Qiao, M. Ye, J. Chen, C. Gao and C.-Y. Guo, *Mater. Lett.*, 2018, **226**, 59–62.

54 M. Yin, L. Yu and S. Liu, *J. Alloys Compd.*, 2017, **696**, 490–497.

55 D. Sánchez-Martínez, C. Gomez-Solis and L. M. Torres-Martinez, *Mater. Res. Bull.*, 2015, **61**, 165–172.

56 Y. Oaki and H. Imai, *Adv. Mater.*, 2006, **18**, 1807–1811.

57 P. J. Boruah, R. R. Khanikar and H. Bailung, *Plasma Chem. Plasma Process.*, 2020, **40**, 1019–1036.

58 A. Wisitsora-at, D. Phokaratkul, K. Jaruwongrangsee, T. M. Daniels and W. Włodarski, *Proceedings*, 2017, **1**, 466.

59 A. Z. Sadek, H. Zheng, M. Breedon, V. Bansal, S. K. Bhargava, K. Latham, J. Zhu, L. Yu, Z. Hu, P. G. Spizzirri, W. Włodarski and K. Kalantar-zadeh, *Langmuir*, 2009, **25**, 9545–9551.

60 M. B. Rahmani, M. H. Yaacob and Y. M. Sabri, *Sens. Actuators, B*, 2017, **251**, 57–64.

61 J. Y. Luo, Z. Cao, F. Chen, L. Li, Y. R. Lin, B. W. Liang, Q. G. Zeng, M. Zhang, X. He and C. Li, *Appl. Surf. Sci.*, 2013, **287**, 270–275.

62 X. Fang, M. Yao, L. Guo, Y. Xu, W. Zhou, M. Zhuo, C. Shi, L. Liu, L. Wang, X. Li and W. Chen, *ACS Sustainable Chem. Eng.*, 2017, **5**, 10735–10743.

63 Y. Hernandez, V. Nicolosi, M. Lotya, F. M. Blighe, Z. Sun, S. De, I. T. McGovern, B. Holland, M. Byrne, Y. K. Gun'Ko, J. J. Boland, P. Niraj, G. Duesberg, S. Krishnamurthy, R. Goodhue, J. Hutchison, V. Scardaci, A. C. Ferrari and J. N. Coleman, *Nat. Nanotechnol.*, 2008, **3**, 563–568.

64 A. O'Neill, U. Khan and J. N. Coleman, *Chem. Mater.*, 2012, **24**, 2414–2421.

65 T. G. Novak, H. Shin, J. Kim, K. Kim, A. Azam, C. V. Nguyen, S. H. Park, J. Y. Song and S. Jeon, *ACS Appl. Mater. Interfaces*, 2018, **10**, 17957–17962.

66 M. Szkoda, Z. Zarach, K. Trzciński, G. Trykowski and A. P. Nowak, *Materials*, 2020, **13**.

67 R. J. Smith, P. J. King, M. Lotya, C. Wirtz, U. Khan, S. De, A. O'Neill, G. S. Duesberg, J. C. Grunlan, G. Moriarty, J. Chen, J. Wang, A. I. Minett, V. Nicolosi and J. N. Coleman, *Adv. Mater.*, 2011, **23**, 3944–3948.

68 D. Xu, P. Xu, Y. Zhu, W. Peng, Y. Li, G. Zhang, F. Zhang, T. E. Mallouk and X. Fan, *ACS Appl. Mater. Interfaces*, 2018, **10**, 2810–2818.

69 D. Pan, Z. Fang, E. Yang, Z. Ning, Q. Zhou, K. Chen, Y. Zheng, Y. Zhang and Y. Shen, *Angew. Chem., Int. Ed.*, 2020, **59**, 16747–16754.

70 T. G. Novak, J. Kim, J. Kim, H. Shin, A. P. Tiwari, J. Y. Song and S. Jeon, *2D Materials*, 2019, **6**, 045019.

71 T. G. Novak, J. Kim, J. Kim, A. P. Tiwari, H. Shin, J. Y. Song and S. Jeon, *Adv. Funct. Mater.*, 2020, **30**, 2001760.

72 J. Kim, N. M. Han, J. Kim, J. Lee, J.-K. Kim and S. Jeon, *ACS Appl. Mater. Interfaces*, 2018, **10**, 37507–37516.

73 Q. Zhang, L. Mei, X. Cao, Y. Tang and Z. Zeng, *J. Mater. Chem. A*, 2020, **8**, 15417–15444.

74 L. Yuwen, H. Yu, X. Yang, J. Zhou, Q. Zhang, Y. Zhang, Z. Luo, S. Su and L. Wang, *Chem. Commun.*, 2016, **52**, 529–532.

75 A. Ghorai, A. Midya, R. Maiti and S. K. Ray, *Dalton Trans.*, 2016, **45**, 14979–14987.

76 P. Zhou, Q. Xu, H. Li, Y. Wang, B. Yan, Y. Zhou, J. Chen, J. Zhang and K. Wang, *Angew. Chem., Int. Ed.*, 2015, **54**, 15226–15230.

77 X.-Y. Tang, M.-F. Li, L.-F. Gao, H. Yan, S.-M. Deng, J.-B. Fan, M.-S. Zheng, S.-L. Deng, Q.-Y. Zhang, S.-Y. Xie and L.-S. Zheng, *Adv. Mater. Interfaces*, 2019, **6**, 1901122.

78 A. Azam, J. Kim, J. Park, T. G. Novak, A. P. Tiwari, S. H. Song, B. Kim and S. Jeon, *Nano Lett.*, 2018, **18**, 5646–5651.

79 T. G. Novak, J. Kim, S. H. Song, G. H. Jun, H. Kim, M. S. Jeong and S. Jeon, *Small*, 2016, **12**, 994–999.

80 S. H. Song, M.-H. Jang, J. Chung, S. H. Jin, B. H. Kim, S.-H. Hur, S. Yoo, Y.-H. Cho and S. Jeon, *Adv. Opt. Mater.*, 2014, **2**, 1016–1023.

81 J. Kim, S. H. Song, H.-G. Im, G. Yoon, D. Lee, C. Choi, J. Kim, B.-S. Bae, K. Kang and S. Jeon, *Small*, 2015, **11**, 3124–3129.

82 S. H. Song, B. H. Kim, D.-H. Choe, J. Kim, D. C. Kim, D. J. Lee, J. M. Kim, K. J. Chang and S. Jeon, *Adv. Mater.*, 2015, **27**, 3152–3158.

83 T. G. Novak, J. Kim, A. P. Tiwari, J. Kim, S. Lee, J. Lee and S. Jeon, *ACS Sustainable Chem. Eng.*, 2020, **8**, 11276–11282.

84 J. B. Mitchell, N. R. Geise, A. R. Paterson, N. C. Osti, Y. Sun, S. Fleischmann, R. Zhang, L. A. Madsen, M. F. Toney, D.-e. Jiang, A. I. Kolesnikov, E. Mamontov and V. Augustyn, *ACS Energy Lett.*, 2019, **4**, 2805–2812.

85 R. Wang, C.-C. Chung, Y. Liu, J. L. Jones and V. Augustyn, *Langmuir*, 2017, **33**, 9314–9323.

86 Z. Wang, W. Gong, X. Wang, Z. Chen, X. Chen, J. Chen, H. Sun, G. Song, S. Cong, F. Geng and Z. Zhao, *ACS Appl. Mater. Interfaces*, 2020, **12**, 33917–33925.

87 K. Kalantar-zadeh, A. Vijayaraghavan, M.-H. Ham, H. Zheng, M. Breedon and M. S. Strano, *Chem. Mater.*, 2010, **22**, 5660–5666.

88 Y. Zhang, Y. Shi, R. Chen, L. Tao, C. Xie, D. Liu, D. Yan and S. Wang, *J. Mater. Chem. A*, 2018, **6**, 23028–23033.

89 L. Liang, J. Zhang, Y. Zhou, J. Xie, X. Zhang, M. Guan, B. Pan and Y. Xie, *Sci. Rep.*, 2013, **3**, 1936.

90 J. Kim, G. Yoon, J. Kim, H. Yoon, J. Baek, J. H. Lee, K. Kang and S. Jeon, *Carbon*, 2018, **139**, 309–316.

91 S.-H. Lee, H. M. Cheong, C. E. Tracy, A. Mascarenhas, J. R. Pitts, G. Jorgensen and S. K. Deb, *Appl. Phys. Lett.*, 2000, **76**, 3908–3910.

92 H. Li, J. Wang, G. Shi, H. Wang, Q. Zhang and Y. Li, *RSC Adv.*, 2015, **5**, 196–201.

93 W. Song, R. Zhang, X. Bai, Q. Jia and H. Ji, *J. Mater. Sci.: Mater. Electron.*, 2020, **31**, 610–620.



94 S. C. Wang, H. J. Chen, G. P. Gao, T. Butburee, M. Q. Lyu, S. Thaweesak, J. H. Yun, A. J. Du, G. Liu and L. Z. Wang, *Nano Energy*, 2016, **24**, 94–102.

95 H. Jin, J. Zhu, W. Chen, Z. Fang, Y. Li, Y. Zhang, X. Huang, K. Ding, L. Ning and W. Chen, *J. Phys. Chem. C*, 2012, **116**, 5067–5075.

96 S. Sallard, T. Brezesinski and B. M. Smarsly, *J. Phys. Chem. C*, 2007, **111**, 7200–7206.

97 S. H. Lee, R. Deshpande, P. A. Parilla, K. M. Jones, B. To, A. H. Mahan and A. C. Dillon, *Adv. Mater.*, 2006, **18**, 763–766.

98 K.-W. Kim, T. Y. Yun, S.-H. You, X. Tang, J. Lee, Y. Seo, Y.-T. Kim, S. H. Kim, H. C. Moon and J. K. Kim, *NPG Asia Mater.*, 2020, **12**, 84.

99 Y. Djaoued, S. Balaji and R. Brüning, *J. Nanomater.*, 2012, **2012**, 674168.

100 S. Chen, Y. Xiao, W. Xie, Y. Wang, Z. Hu, W. Zhang and H. Zhao, *Nanomaterials*, 2018, **8**, 553.

101 W. Yu, Z. Shen, F. Peng, Y. Lu, M. Ge, X. Fu, Y. Sun, X. Chen and N. Dai, *RSC Adv.*, 2019, **9**, 7723–7728.

102 J. Yan, T. Wang, G. Wu, W. Dai, N. Guan, L. Li and J. Gong, *Adv. Mater.*, 2015, **27**, 1580–1586.

103 J.-J. Li, M. Zhang, B. Weng, X. Chen, J. Chen and H.-P. Jia, *Appl. Surf. Sci.*, 2020, **507**, 145133.

104 W. Kong, R. Zhang, X. Zhang, L. Ji, G. Yu, T. Wang, Y. Luo, X. Shi, Y. Xu and X. Sun, *Nanoscale*, 2019, **11**, 19274–19277.

105 Y. Qin and Z. Ye, *Sens. Actuators, B*, 2016, **222**, 499–507.

106 A. Staerz, S. Somacescu, M. Epifani, T. Kida, U. Weimar and N. Barsan, *ACS Sens.*, 2020, **5**, 1624–1633.

107 C.-Y. Wang, X. Zhang, Q. Rong, N.-N. Hou and H.-Q. Yu, *Chemosphere*, 2018, **204**, 202–209.

108 X. Zhou, X. Zheng, B. Yan, T. Xu and Q. Xu, *Appl. Surf. Sci.*, 2017, **400**, 57–63.

109 C.-C. Liao, F.-R. Chen and J.-J. Kai, *Sol. Energy Mater. Sol. Cells*, 2006, **90**, 1147–1155.

110 H. Yu, J. Guo, C. Wang, J. Zhang, J. Liu, G. Dong, X. Zhong and X. Diao, *Electrochim. Acta*, 2020, **332**, 135504.

111 Q. Xu, L. Zhang, B. Cheng, J. Fan and J. Yu, *Chem.*, 2020, **6**, 1543–1559.

112 S. Singh, J. Deb, U. Sarkar and S. Sharma, *ACS Appl. Nano Mater.*, 2021, **4**, 2594–2605.

113 Y. Han, Y. Liu, C. Su, X. Chen, B. Li, W. Jiang, M. Zeng, N. Hu, Y. Su, Z. Zhou, Z.-g. Zhu and Z. Yang, *ACS Appl. Nano Mater.*, 2021, **4**, 1626–1634.

114 Y. Zheng, L. Sun, W. Liu, C. Wang, Z. Dai and F. Ma, *J. Mater. Chem. C*, 2020, **8**, 4206–4214.

115 C. Wang, S. Zhang, L. Qiu, S. A. Rasaki, F. Qu, T. Thomas, Y. Liu and M. Yang, *J. Alloys Compd.*, 2020, **826**, 154196.

116 M. Yin, Y. Yao, H. Fan and S. Liu, *J. Alloys Compd.*, 2018, **736**, 322–331.

117 Y. Gui, L. Yang, K. Tian, H. Zhang and S. Fang, *Sens. Actuators, B*, 2019, **288**, 104–112.

118 R. Samal, B. Chakraborty, M. Saxena, D. J. Late and C. S. Rout, *ACS Sustainable Chem. Eng.*, 2019, **7**, 2350–2359.

119 S. Chaitoglou, R. Amade and E. Bertran, *Nanoscale Res. Lett.*, 2017, **12**, 635.

120 S. K. Park, H. J. Lee, M. H. Lee and H. S. Park, *Chem. Eng. J.*, 2015, **281**, 724–729.

121 W. Dang, W. Wang, Y. Yang, Y. Wang, J. Huang, X. Fang, L. Wu, Z. Rong, X. Chen, X. Li, L. Huang and X. Tang, *Electrochim. Acta*, 2019, **313**, 99–108.

122 S. B. Ambade, R. B. Ambade, W. Eom, S. H. Noh, S. H. Kim and T. H. Han, *Adv. Mater. Interfaces*, 2018, **5**, 1801361.

